

1 **Nuclear transport under stress phenocopies transport defects in models of**
2 **C9Orf72 ALS**

3
4 Marije F.W. Semmelink¹, Hamidreza Jafarinia², Justina C Wolters³, Teodora Gheorghe¹, Sara N. Mouton¹, Anton
5 Steen¹, Patrick R. Onck², Liesbeth M. Veenhoff¹

6 ¹ European Research Institute for the Biology of Ageing, University of Groningen, University Medical
7 Center Groningen, 9713 AV Groningen, The Netherlands

8 ² Zernike Institute for Advanced Materials, University of Groningen, Nijenborgh 4, Groningen 9747
9 AG, The Netherlands.

10 ³ Department of Pediatrics, Section Systems Medicine of Metabolism & Signaling, University of
11 Groningen, University Medical Center Groningen, 9713 AV Groningen, The Netherlands.

12 To whom correspondence should be addressed: l.m.veenhoff@rug.nl

13
14 Keywords: Nuclear transport, Nuclear Pore Complex, Nuclear Transport Receptor, C9Orf72, amyotrophic lateral
15 sclerosis (ALS), Stress

16
17
18

19 **Abstract**

20 The nucleus is the hallmark of eukaryotic life and transport to and from the nucleus occurs through
21 the nuclear pore complex (NPC). There is a multitude of data connecting the nuclear transport
22 machinery – i.e. the NPCs and associated nuclear transport factors - to neurodegenerative diseases,
23 but the mechanisms are not well understood. Using *Saccharomyces cerevisiae*, we systematically
24 studied how the expression of polyPR and polyGA related to C9Orf72 amyotrophic lateral sclerosis
25 impacts the nuclear transport machinery. We measured the abundance and localization of NPC
26 components and transport factors, and assessed the kinetics of import and export by four transport
27 receptors. PolyPR and polyGA cause distinct, and transport receptor dependent effects. We compared
28 the specific changes in transport to those obtained when cells were exposed to different stress
29 situations or mutations. This comparison showed similar patterns of transport defects in cells lacking
30 specific NTRs and cells expressing polyPR. In contrast, polyGA expressing cells bear resemblance to
31 stress conditions where energy maintenance is decreased. The similarity of the patterns of transport
32 deficiencies suggests that polyPR has a direct effect on nuclear transport via NTRs, while polyGA
33 impacts the energy state of the cell and subsequently changes transport.

34

35 **Abbreviations:**

36 C9ALS	Chromosome 9 Amyotrophic Lateral Sclerosis
37 DPRs	DiPeptide Repeat proteins
38 FG-Nup	phenylalanine–glycine repeat containing Nup
39 FUS	Fused in Sarcoma
40 GA/GP/GR/PA/PR	Glycine-Alanine, Glycine-Proline, Glycine-Arginine, Proline-Alanine, Proline-Arginine
41 NCT	NucleoCytoplasmic Transport
42 NES	Nuclear Export Signal
43 NLS	Nuclear Localization Signal
44 NPC	Nuclear Pore Complex
45 NTF	Nuclear Transport Factor
46 NTR	Nuclear Transport Receptors
47 Nup	Nucleoporin
48 RAN translation	Repeat-Associated Non-AUG translation
49 ROS	Reactive Oxygen Species
50 TDP43	TAR DNA-binding protein-43

51 Introduction

52 Nucleocytoplasmic transport

53 For all eukaryotes, DNA is safely stored in their nuclei, which allows for compartmentalization of
54 transcription and translation, thereby contributing to the control of gene expression. The nuclear
55 envelope separates the contents of the nucleus from the cytoplasm, and contains nuclear pore
56 complexes (NPCs) which perform highly regulated transport as well as passive diffusion through their
57 permeability barrier. The NPCs are large protein complexes build from nucleoporins (Nups), with
58 roughly half of the mass of an NPC constituted by Nups containing phenylalanine-glycine repeats (FG-
59 Nups)¹. Additionally, a pool of Importin- β functions as a stable component of the NPC's permeability
60 barrier². Nucleocytoplasmic transport (NCT) through the pores is performed by several nuclear
61 transport receptors (NTRs) and together they bind a large and diverse group of cargoes. While general
62 protein export is mediated only by the major exportin Crm1, different importins are jointly responsible
63 for all protein import. Baker's yeast contains 18 known NTRs, whereas in human cells 30 NTRs have
64 been identified³⁻⁷. The Importin- β superfamily is the largest class of NTRs; they can either directly bind
65 to their cargo, or via an adaptor protein, an Importin- α isoform⁸. Cargo recognition is achieved via
66 either a nuclear localization signal (NLS) which binds to an importin, or a nuclear export signal (NES)
67 which binds to an exportin. For the NTRs some, but not all, cargoes are known, and redundancies exist⁹.
68 The directionality of the transport is maintained by a gradient of Ran, a member of the Ras family of
69 small GTPases, which is bound to GTP in the nucleus and to GDP in the cytoplasm. Importins require
70 RanGTP to dissociate from their cargo in the nucleus, and exportins require RanGTP to bind
71 simultaneously with their cargo to allow binding¹⁰⁻¹².

72

73 Transport in neurodegeneration and under stress conditions

74 Nuclear transport of transcriptional regulators is a key step in responding to stress. For example, it was
75 shown that transport by specific NTRs increases or decreases in response to heat shock¹³⁻¹⁶, glucose
76 deprivation¹⁷⁻²⁰, osmotic shock^{21,22}, or oxidative stress^{15,23-26}. Neurodegenerative diseases are also
77 linked to alterations in NCT. This may be indirect, for example via the mentioned stress responses, or
78 the connection may be more direct through interactions of the disease proteins with the NPC
79 components or nuclear transport factors. E.g. mutant Huntingtin, co-aggregates Nups and RanGAP,
80 reduces the abundance of nuclear RanGTP, and reduces protein import and export²⁷. Alzheimer's
81 related tau protein also mislocalizes Nups and Ran, changes NPC permeability, and protein import and
82 export²⁸. The mutant form of TDP-43 (TAR DNA-binding protein-43) aggregates and is linked to ALS. Its
83 aggregation triggers the mislocalization of Nups and NTRs, and interferes with protein import and RNA
84 export²⁹. Mutations in the NLS of the Fused in Sarcoma (FUS) protein reduce binding to its importin,
85 and cause aggregation in cytoplasmic stress granules in FUS-related ALS³⁰. Alteration of protein import
86 and export was also seen in the presence of non-natural, synthetic β -sheet proteins, which suggests
87 protein aggregation in general may be linked to reduced NCT³¹.

88

89 A specific type of ALS is caused by a repeat-expansion of G₄C₂ in *C9orf72* (C9ALS), which leads to
90 disruption of the *C9orf72* intron and thus a loss of function of the *C9orf72* protein. In addition, the
91 repeat RNA may cause a toxic gain of function, and, the extended G₄C₂ repeats leads to unconventional
92 repeat-associated non-AUG (RAN) translation. This non-canonical initiation of translation allows
93 elongation of a repeat sequence in the absence of an AUG starting codon, in multiple reading frames,
94 and so generates multiple dipeptide repeat proteins (DPRs)³². For *C9orf72*, the sense RNA encodes
95 glycine-alanine (GA), glycine-proline (GP), and glycine-arginine (GR) repeat proteins. The antisense
96 transcript produces proline-arginine (PR), GP, and proline-alanine (PA)^{33,34} repeat proteins. Of these
97 DPRs, polyPR is the most toxic species in most studied models³⁵⁻³⁹, followed by polyGR, while polyGA
98 is toxic in about half the models, and polyPA is never toxic (reviewed in⁴⁰).

99

100 The underlying cause for toxicity in C9ALS is still unknown, but interaction with NCT was shown in
101 multiple studies (reviewed in⁴¹⁻⁴⁵). The *C9orf72* protein was found to interact with both Importin β 1

102 and Ran-GTPase⁴⁶. (G₄C₂)₃₀ RNA was shown to directly bind to RanGAP⁴⁷, and polyGA was reported to
103 bind RanGAP1 in cytoplasmic inclusions⁴⁸, and to reduce NCT⁴⁹. The toxicity of (G₄C₂)₅₈ was further
104 linked to impaired RNA export, and moreover knockout or overexpression of many nuclear transport
105 proteins was found to influence neurodegeneration⁵⁰. Direct binding of PR to one of the NTRs,
106 importin- β , resulted in decreased nuclear import of importin β , importin α/β , and transportin cargoes
107 in permeabilized mouse neurons and HeLa cells⁵¹. In addition, nuclear envelopes incubated with PR₂₀
108 peptides showed polyPR presence in the main channel of NPCs⁵². Furthermore, the distribution of
109 protein components of NPCs were found to be altered in ALS patients and ALS mouse models⁵³. Indeed,
110 there is evidence to support that NPC quality control is compromised in ALS patients⁵⁴. However, the
111 studies addressing whether transport is altered in these C9ALS models have provided different
112 answers, which can, at least in part, be explained by the differences in the methods used to study
113 transport^{29,47,51,52,55-58} (reviewed in⁴⁰). For example, it was shown that G₄C₂-repeats decrease importin
114 α/β transport^{29,47,51}, as do PR₂₀ peptides⁵² and GR₂₅⁵⁵. In contrast, others only see an effect on importin
115 α/β transport in the presence of GA₁₄₉-GFP, and not with GFP-GR₁₄₉ or PR₁₇₅-GFP⁵⁶, or determined none
116 of the DPRs impacted importin α/β transport⁵⁷. Also, in the presence of polyPR, the transport of the
117 human NTR Transportin (TNPO1) was shown to be unchanged in some studies^{56,57}, but reduced in
118 another⁵¹.

119
120 Thus, while NCT and C9Orf72 ALS have been convincingly linked in literature, there are only few studies
121 that directly address the changes in the kinetics of nuclear transport and the outcomes are not uniform
122 nor comprehensive. Therefore, a clear answer to the question whether and how much the kinetics of
123 nuclear transport of *all* proteins is impacted, has not been given. This is an important question because,
124 if true, then a global derailment of protein localization should be expected in patients; a derailment
125 that could only be solved at the level of interfering with the NCT machinery. However, it is also possible
126 that the thus far reported connections are not a reflection of generally impaired nuclear transport
127 kinetics, but rather a result of the mislocalization or aggregation of specific proteins that subsequently
128 cause the mislocalization of a small subset of interacting proteins. Another outstanding question is
129 whether transport defects are an effect of direct interaction of the disease-causing proteins with the
130 nuclear transport machinery, or rather an indirect result from stress caused by these disease proteins.
131 Here we take a reductionist approach and seek to answer these questions for simple models of polyPR
132 or polyGA expressing yeast cells, measuring the changes in transport kinetics of four transport factors
133 and comparing them to those measured under different stress conditions.

134

135 Results

136 Characterizing the components of the nuclear transport machinery in yeast C9ALS models

137 To study the effects of C9ALS DPRs on transport, we used a yeast model expressing 50 repeats of PR
138 or GA, developed by³⁵. 50 repeats is lower than common in ALS patients, but similar to previous studies
139 (ranging between 10-65 repeats^{35,38,39,48,49,51,55,59,60}) including a mouse model with 66 repeats which
140 recapitulates molecular and behavioural abnormalities of C9ALS patients⁶¹. In accordance with
141 previous studies³⁵⁻³⁹, the yeast cells expressing polyPR, but not those expressing polyGA, have a growth
142 defect, as shown by the limited growth in a spot assay (Fig 1A). The reduced growth on plate by polyPR
143 was validated by following individual dividing cells in microfluidic chips (ALCATRAS system as
144 described⁶²): we see that polyPR expressing cells have a median replicative lifespan of only two
145 divisions, compared to a lifespan of eighteen cell divisions of WT cells (Fig 1B). In order to determine
146 the localization of both DPRs, we tagged them (N-terminally) with mCerulean. This somewhat reduces
147 the toxicity of polyPR, resulting in a median of six cell divisions (Fig 1B). mCerulean-polyPR is mostly
148 nucleolar, since it co-localizes with the nucleolar protein Sik1, consistent with previous reports in other
149 models^{36-39,60} (Fig 1C). PolyGA forms a rod-shaped focus in the cytoplasm (Fig 1C), which is also
150 observed in other models^{38,48,59,63-65}. Altogether, we conclude that our yeast model recapitulates basic
151 features of toxicity and subcellular localization of the polyPR and polyGA DPRs as observed in other
152 models.

153 In order to determine whether the transport machinery components are altered in our model, we
154 systematically studied the abundance and localization of the NTRs, the components of the NPC and
155 those generating the Ran cycle (selection of NTRs and nucleoporins in Fig 2 and others in Fig 2 -
156 supplement figures 1/2/3). First, we assessed the NTRs in our model. Alterations in the concentration
157 of importing NTRs will change the transport kinetics, since the import rate of cargo is limited by the
158 formation of NTR-cargo complexes in the cytosol⁶⁶⁻⁶⁸. Using SRM-based proteomics, we determined
159 that the expression levels of the 18 NTRs found in yeast⁵ were similar in WT and polyPR or polyGA
160 expressing cells (Fig 2 and Fig 2 – figure supplement 1A). To investigate the localization of these NTRs,
161 we expressed PR₅₀ or GA₅₀ in strains expressing endogenously GFP-tagged NTRs, and were able to
162 probe 16 out of the 18 yeast NTRs⁵ (Mtr2 and Ntf2 were unavailable). In general, we find no evidence
163 that the localization of GFP-tagged NTRs is significantly altered upon expression of the DPRs. Small
164 differences may be present in the localization of Pse1, which forms fewer nuclear envelope localized
165 foci with both DPRs, and in the localization of Cse1, which is less abundant at the NE with PR₅₀-
166 expression (Fig 2 and Fig 2 – figure supplement 1B/C/D). Importantly, none of the NTRs accumulated
167 visibly either in the nucleolus with polyPR, or in the cytoplasmic aggregate of polyGA. Jointly the
168 analysis shows that expression of polyPR or polyGA does not inflict major changes in the abundance
169 and localization of NTRs.
170

171 Next, we assessed if there may be changes in the total number of NPCs in our ALS models. We
172 measured the abundance of all nucleoporins in a proteomics analysis and found no expression level
173 changes (Fig 2 and Fig 2 – figure supplement 2A). Also, the localization of four endogenously expressed
174 GFP-tagged nucleoporins was assessed, and we see no relocation of the FG-Nups Nsp1 and Nup159,
175 outer ring Nup133, nor the linker nucleoporin Nic96 (Fig 2 and Fig 2 – figure supplement 2B). Obviously,
176 these measurements cannot report on the functional state of these NPCs, but the data does suggest
177 that the expression of polyPR or polyGA does not majorly alter the numbers of NPCs.
178

179 Another major component of nucleocytoplasmic transport is the Ran cycle, which maintains the
180 directionality of transport. Previous studies showed that the toxicity caused by (GGGGCC)_n RNA and
181 poly-GR/PR is exacerbated when Ran and/or RanGAP1 are knocked down in *Drosophila* and
182 yeast^{35,47,50,69}. Co-localization of poly-GA aggregates with RanGAP1 has also been reported⁴⁸, but this
183 was not observed for Ran or RanGAP1 in another study⁵⁶. In order to determine whether DPR
184 expression changes the Ran cycle in our yeast model, we expressed endogenously tagged RanGAP-
185 GFP, and its nuclear counterpart RanGEF-GFP, together with polyPR or polyGA. We did not observe
186 any change in localization of either RanGAP or RanGEF (Fig 2 and Fig 2 – figure supplement 3A).
187 Proteomics analysis shows that the total abundance of both RanGAP and RanGEF is possibly
188 upregulated (a 1,5x fold increase is measured) in PR₅₀ expressing cells, and unchanged in polyGA
189 expressing cells (Fig 2 – figure supplement 3B). To assess if this change in RanGAP and RanGEF levels
190 is associated with a change in energy levels, we measured cellular ATP levels with a FRET-based ATP-
191 sensor (adapted from the AT1.03 ATP biosensor⁷⁰). We find that the free ATP concentration is not
192 altered in polyPR and polyGA expressing cells (Fig 2 and Fig 2 – figure supplement 3C). Since a depletion
193 of ATP was shown previously to cause a drop in free GTP levels⁷¹, our measurement of stable ATP levels
194 may indicate that also GTP levels are unchanged in polyPR and polyGA expressing cells.
195

196 In summary, our yeast model recapitulates the toxicity and localization of the DPRs polyPR and polyGA
197 as reported in other models. Our analysis shows that the abundance and localization of NTRs,
198 nucleoporins, and thus also NPCs, are unaltered upon expression of polyPR or polyGA. In PR₅₀
199 expressing cells a small upregulation of RanGAP and RanGEF was measured, but at least energy levels
200 as measured via free ATP levels are unchanged. Having characterized the components of the nuclear
201 transport machinery in the yeast ALS models, we next study whether transport is affected by either
202 polyPR or polyGA expression.
203
204

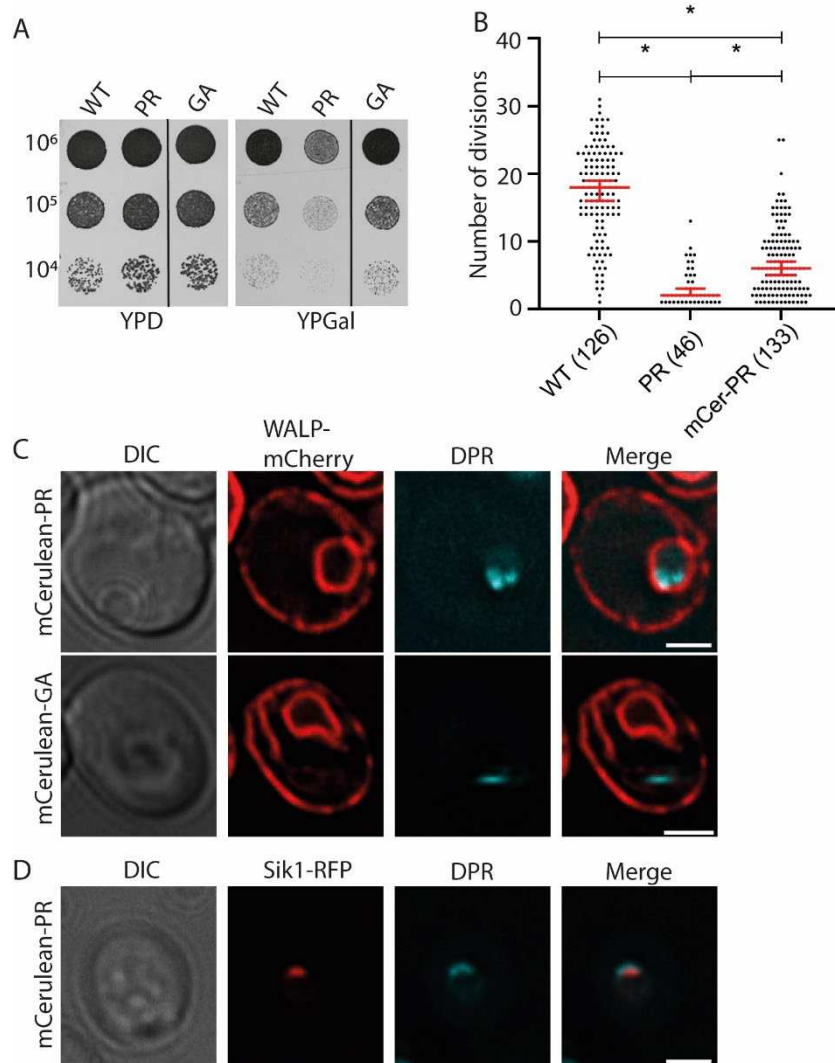
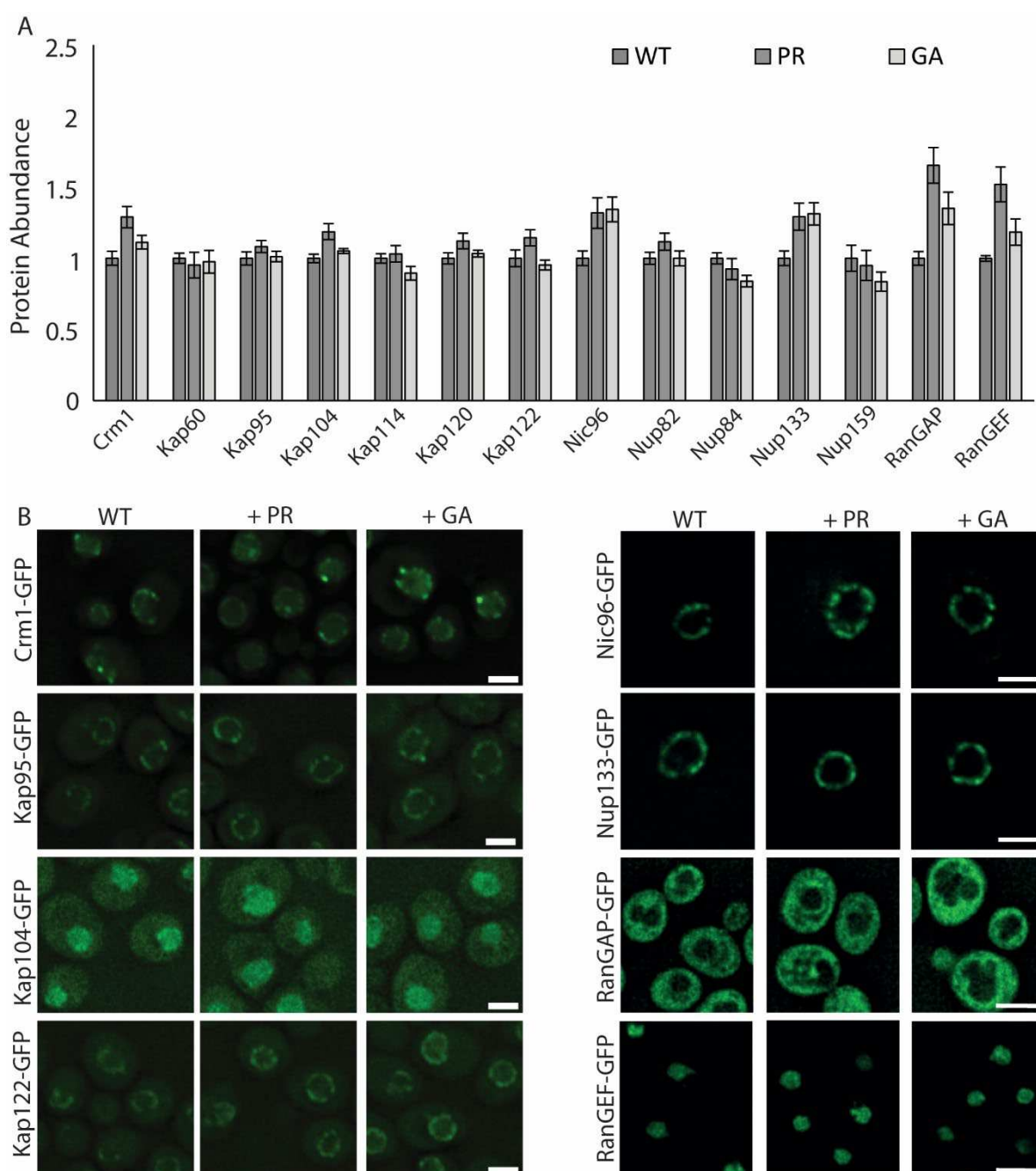


Fig 1. Yeast models for C9Orf72 ALS: expression of polyPR and poly-GA. A) PR₅₀ is toxic under conditions when expression is induced while GA₅₀ is not toxic. Left panel, uninduced (glucose), right panel, induced (galactose). **B)** Replicative lifespan of cells expressing PR₅₀ or mCerulean-tagged PR₅₀ (mCer-PR) in ALCATRAS chip compared to WT. Numbers of cells followed throughout their lifespan is indicated; data set from wild type cells taken from our previous work⁷². **C)** mCerulean-PR₅₀ localizes in the nucleus, whereas mCerulean-GA₅₀ localizes in a cytoplasmic focus. WALP-mCherry indicates the NE-ER network (in red). **D)** mCerulean-PR₅₀ co-localizes with the nucleolar protein Sik1/Nop56-RFP, shown in red. Scale bar equals 2μm.



214
215 **Fig 2. Abundance and localization of selected NTRs, Nups and the Ran system in polyPR and polyGA expressing cells.** For
216 other NTRs and Nups please see Figure Supplement 1,2,3. **A)** Abundance of few of the NTRs, Nups and RanGEF and RanGAP
217 in whole cell extracts of WT or PR₅₀/GA₅₀-expressing cells determined by SRM-based proteomics in two biological and one
218 technical replicate, source data 1. **B)** Localization of endogenously GFP-tagged NTRs compared between WT cells and cells
219 expressing PR₅₀ or GA₅₀; scale bar equals 2 μm.

220
221 Does expression of polyPR and polyGA change import and export?
222 Having characterized the abundance and localization of the main players in NCT, we next determined
223 the effect of DPRs on two functional read-outs for nuclear transport^{73,74}, namely the rate of passive
224 diffusion and the rate of active transport through the pores. For mobile proteins, the balance between
225 NTR-facilitated import of NLS-containing proteins and their passive efflux leads to nuclear
226 accumulation. Similarly, the balance of NTR-facilitated export of proteins with an NES and their passive
227 influx leads to a steady-state nuclear exclusion (Fig 3A). Not all NTRs and their NLS/NESs are known,
228 and in this study we have used i) the Stress-Severity subfamily B1 NES (NES_{Ssb1}⁷⁵) for the Crm1 exportin,
229 ii) the monopartite, classical Simian Virus 40 NLS (NLS_{SV40}⁷⁶) for the Kap60/Kap95 import complex, iii)

230 the bipartite nucleophosmin (Npm1) NLS (NLS_{Npm1}⁷⁷) also for the Kap60/Kap95 import complex, iv) the
231 Nuclear polyAdenylylated RNA-Binding 2 NLS (NLS_{Nab2}⁷⁸) for Kap104, and v) the PHOspate metabolism
232 4 NLS (NLS_{Pho4}⁷⁹) for Kap121/Pse1 (Table 1 and more details in Table S1).

233

Table 1 NLSs and NTRs

NLS	Ssb1 NES	Sv40 NLS	Npm1 NLS	Nab2 NLS	Pho4 NLS
Karyopherin	Crm1	Kap60/95	Kap60/95	Kap104	PSE1

234

235 To monitor the effect of PR₅₀ or GA₅₀ on nuclear transport, we quantified the steady state localization
236 of GFP-NLS reporter proteins encoding the NLSs specific to Kap60/95, Kap104, and Pse1, and a GFP-
237 NES reporter recognized by Crm1 (summarized in table S1, and Fig 3B) in cells expressing PR₅₀ or GA₅₀.
238 As a control for the reporter proteins, we included GFP without sorting signals. The steady state
239 distribution of the GFP-reporters is calculated by taking the ratio of the fluorescence measured in the
240 nucleus and the cytosol (the N/C ratio). GFP accumulates slightly in the nucleus due to its hydrophobic
241 surface properties⁸⁰, represented by a median N/C ratio of 1.24 ± 0.14 in WT cells (Fig 3C, and table
242 S2). The N/C ratio of GFP is identical in cells expressing PR₅₀, and slightly lower in GA₅₀ expressing cells
243 (median N/C ratio to 1.11 ± 0.11). The import reporters accumulate in the nucleus, and thus have an
244 N/C ratio >1, whereas the export reporter is excluded from the nucleus and has an N/C ratio <1 (Fig
245 3B). Please note that when nuclear export decreases, the N/C ratio will increase and approach the
246 value of 1. We interpret a decrease in steady state nuclear localization of the import reporter as a
247 decrease in the import kinetics by this NTR. This interpretation holds under the assumption that the
248 import of native cargo's (that compete with the reporter for the same pool of NTR⁸¹) is stable under
249 the conditions we compared. Support for this comes from proteomics data showing that the
250 abundance of a few known cargoes of the NTRs involved (Kap95, Kap104, Pse1 and Crm1) are not
251 altered upon DPR expression (Source data 2). In addition, our data (Fig S1A) and previous studies
252 following the transport of GFP-NLS reporter proteins⁶⁷, suggest that the NTR availability is not limiting
253 under the conditions used.

254

255 We first addressed if expression of the DPRs alters the passive permeability of the pore. For this we
256 measured the immediate loss of nuclear accumulation of import reporters carrying the Sv40, Nab2 or
257 Pho4 NLS after inhibiting active transport (Fig 3D). The inhibition of active transport is achieved by
258 poisoning the cells with sodium azide and 2-deoxy-D-glucose, which respectively inhibit the
259 mitochondrial respiratory chain and glycolysis. The analysis showed that the expression of PR or GA
260 resulted in minimal changes in leak rate for the NLS_{Sv40}-, NLS_{Nab2}- and NLS_{Pho4}-GFP reporter (Fig 3E, table
261 S3).

262

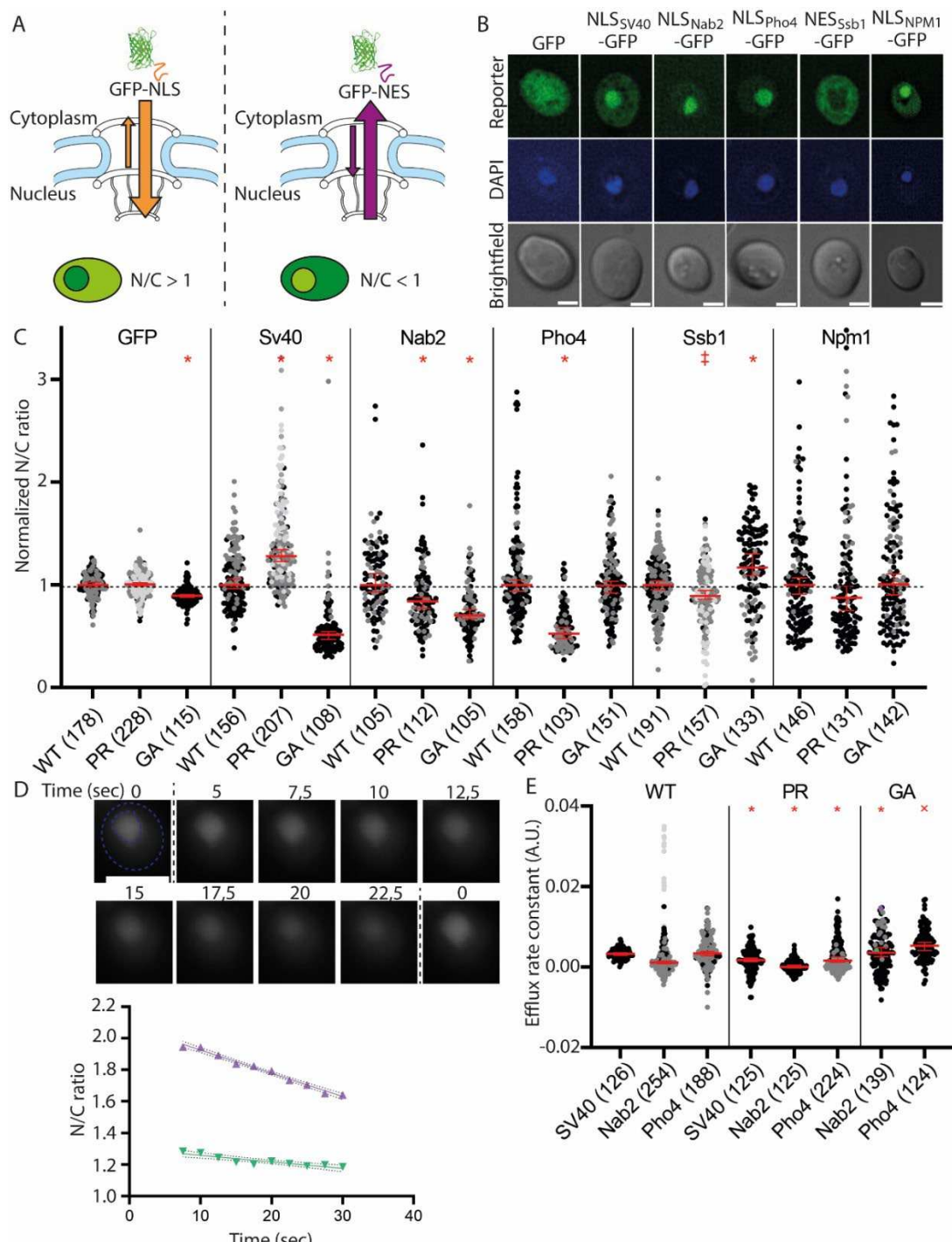
263 Having established that polyPR or polyGA expression gives only minor changes in passive permeability
264 of NPCs, we measure the steady state localization of import and export reporters to probe also the
265 active transport rates. Assessing the effects of polyPR expression we see that the nuclear exclusion of
266 NES_{Ssb1}-GFP and the nuclear accumulation of NLS_{Sv40}-GFP are both modestly but significantly increased
267 when PR₅₀ is expressed. However, the NLS_{NPM1} reporter is not significantly affected by polyPR
268 expression, showing that even for one transport route, i.e. via the Kap60/95 complex, different effects
269 are observed for specific NLSs. In contrast, a loss of compartmentalization is observed for the reporters
270 carrying the NLS_{Nab2} or the NLS_{Pho4}. The effects on transport caused by polyGA expression are distinct:
271 export is reduced in polyGA expressing cells, and import of the NLS_{Sv40}-GFP and NLS_{Nab2}-GFP are also
272 decreased (Fig 3C and table S2). The nuclear accumulation of both the NLS_{Pho4}-GFP and the NLS_{NPM1}-
273 GFP reporter is unaffected. It is interesting that for both polyPR and polyGA expression, despite the
274 variation observed in the other transport routes, the NPM1 reporter (carrying a bipartite NLS) is
275 unaffected.

276

277 In short, the transport measurements jointly show that polyPR increases the transport of the classical
 278 NLS_{SV40}, and the NES_{Ssb1}, but decreases transport of the other two import routes. PolyGA reduces
 279 transport of the NLS_{SV40}, NLS_{Nab2}, and NES_{Ssb1}. Thus, the analysis highlights that DPR expression impacts
 280 the transport facilitated by different NTRs, and even by NLSs for the same NTR, and that to varying
 281 degree and direction.

282

283



284

285 **Fig 3. Steady-state N/C ratios of transport reporters are altered with polyPR and polyGA expression.** A) Nuclear
 286 accumulation or exclusion are the result of active import and passive leakage resulting in nuclear accumulation for the NLS-
 287 reporter, and the opposite for the NES-reporter. B) Subcellular distribution of the GFP-reporters in wildtype cells, nuclear
 288 staining DAPI, scale bar equals 2 μ m. C) N/C ratios of GFP-transport reporters in WT, PR₅₀ or GA₅₀-expressing cells,
 289 determined in 2-4 independent experiments (grey colours); total number of cells analysed between brackets, source data 3.
 290 Data is normalized to the median WT values for each reporter, median and 95% confidence interval are shown in red, Mann-

291 Whitney comparison to WT with \ddagger = p-value <0.01, and * = p-value <0.0001. A total of 10 datapoints with normalized N/C
292 above 3.5 are not shown but taken into account in the statistics (respectively 1,1,1,2 and 5 points for the datasets *SV40-PR*,
293 *Pho4-WT*, *Pho4-GA*, *NPM1-PR* and *NPM1-GA*). **D**) Measurements of transport reporters nuclear accumulation loss and
294 calculated efflux kinetics. Time zero is the time point at which the metabolic poisons (Na-azide and 2-deoxy-glucose) reached
295 the cells and active transport of the reporters stops. N/C ratios were recorded 5-22,5 sec after poisoning occurred, after which
296 linear regression slopes were determined. Green triangles show a cell with average efflux rate constant of -0,0041; purple
297 triangles show the presented cell with a particularly strong reduction of the N/C ratio of -0,014. **E**) Efflux rate constants in WT
298 and ployPR and polyGA expressing cells, data from independent experiments are shown in different grey colours, with the
299 median and 95% confidence interval in red, Mann-Whitney comparison to WT with x = p-value <0.001, and * = p-value
300 <0.0001.

301

302 Nuclear transport under stress conditions

303 So far, our analysis established that DPR expression impacts the transport kinetics by different NTRs,
304 but it is not clear if we should consider these changes to be small or large. To provide a context for the
305 quantitative assessment of transport defects, we compare them to those measured under several
306 stress conditions. We subjected yeast to diverse stressors, namely heat shock, starvation, osmotic
307 shock, and oxidative stress, and determined the effect on transport.

308 Upon mild heat shock at 37°C for 5 minutes, classical import (NLS_{SV40}) and classical export (NES_{Ssb1}) are
309 not changed, but import of the NLS_{Nab2} - and NLS_{Pho4} -GFP reporters is reduced (Fig 4B, table S4). If cells
310 are kept at mild heat shock for an hour, they adapt to the stress and the import by all three importins
311 goes up again, even increasing above wild type levels. This overshoot effect is the strongest for the
312 NLS_{Pho4} -GFP reporter. Interestingly, increasing the heat shock to severe temperatures – i.e. 42°C for 5
313 minutes – shows decreased import of the NLS_{SV40} -reporter, but now the NLS_{Pho4} -reporter is not
314 affected. Under sublethal heat shock at 46°C for 10min the differences between the import routes
315 become even larger, where import of the NLS_{SV40} -reporter is further reduced compared to 42°C, import
316 of the NLS_{Nab2} -reporter is increased, and the NLS_{Pho4} -reporter is not affected. Also interesting is that
317 the NLS_{Pho4} -reporter is only impacted at 37°C, but under higher temperatures import is not affected.
318 Next, we subjected the cells to two different methods of starvation. When cells pass the diauxic shift,
319 after growing to saturation, we see a decrease in import of the NLS_{SV40} -reporter, and a decrease in
320 export of the NES_{Ssb1} -reporter after 20 hours in medium (Fig 4C and table S4). The transport of the
321 other two import reporters is not significantly decreased. In contrast, after 24h in water, all three
322 import routes, as well as export are reduced. Thus, import by these three pathways is more susceptible
323 to water shift, whereas the impact of saturated growth is stronger on export.

324 Next we assessed the response to an osmotic shock with 1M NaCl (as in⁸²) (Fig 4D, table S4). We see
325 that both the NLS_{SV40} - and NLS_{Pho4} -reporter are less accumulated under osmotic shock. The NLS_{Nab2} -
326 reporter is not significantly impacted, and the export of the NES -reporter is drastically impaired.

327 A last set of stresses induces oxidative stress, either by means of the addition of 4mM hydrogen
328 peroxide, or via the intracellular production of reactive oxygen species (ROS) after 40 minutes exposure
329 to 1,2mM menadione. Peroxide stress reduces import of all three different reporters, but export is not
330 affected (Fig 4E, table S4). Hydrogen peroxide, being highly reactive, will only temporarily generate
331 ROS, and indeed 30 minutes after the addition of hydrogen peroxide the cells return to normal
332 transport phenotypes. Similar to what we saw with adaptation to mild heat stress, classical import
333 “overshoots” the normal accumulation and even increases import a little over the wild type situation.
334 ROS created by incubation with menadione completely abolished active transport: the N/C ratios of
335 the import reporters are all reduced to roughly 1. Export is drastically reduced, similarly to osmotic
336 stress, but the N/C ratios are still below 1.

337 Lastly, incubation of the cells with 15% ethanol for 20 minutes reduced import strongly, although it is
338 not abolished and N/C ratios are still above 2 (Fig 4F, table S4). Export is completely inhibited, and the
339 N/C ratio reaches 1.

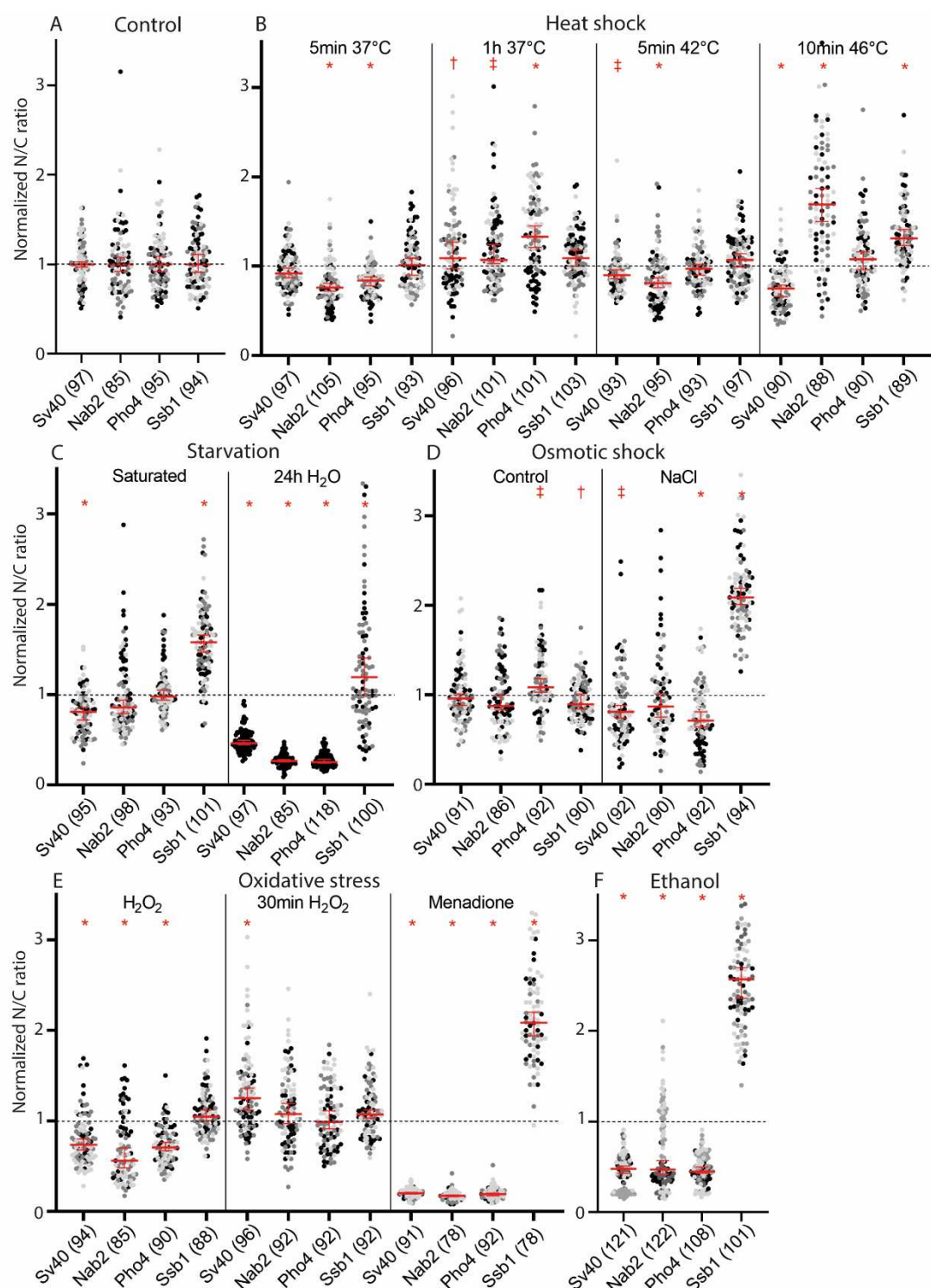
340 In conclusion, we have quantified transport by four NTRs under twelve different environmental
341 stressors. Our findings align with previous work in yeast¹⁸ measuring the transport by one NTR
342 (Kap60/95) in stationary phase culture, and in conditions of exposure to ethanol, oxidative stress, heat

343 stress, and adaptation to heat stress. They are different for those measured in condition of osmotic
344 shock; possibly due to differences in the model¹⁸.

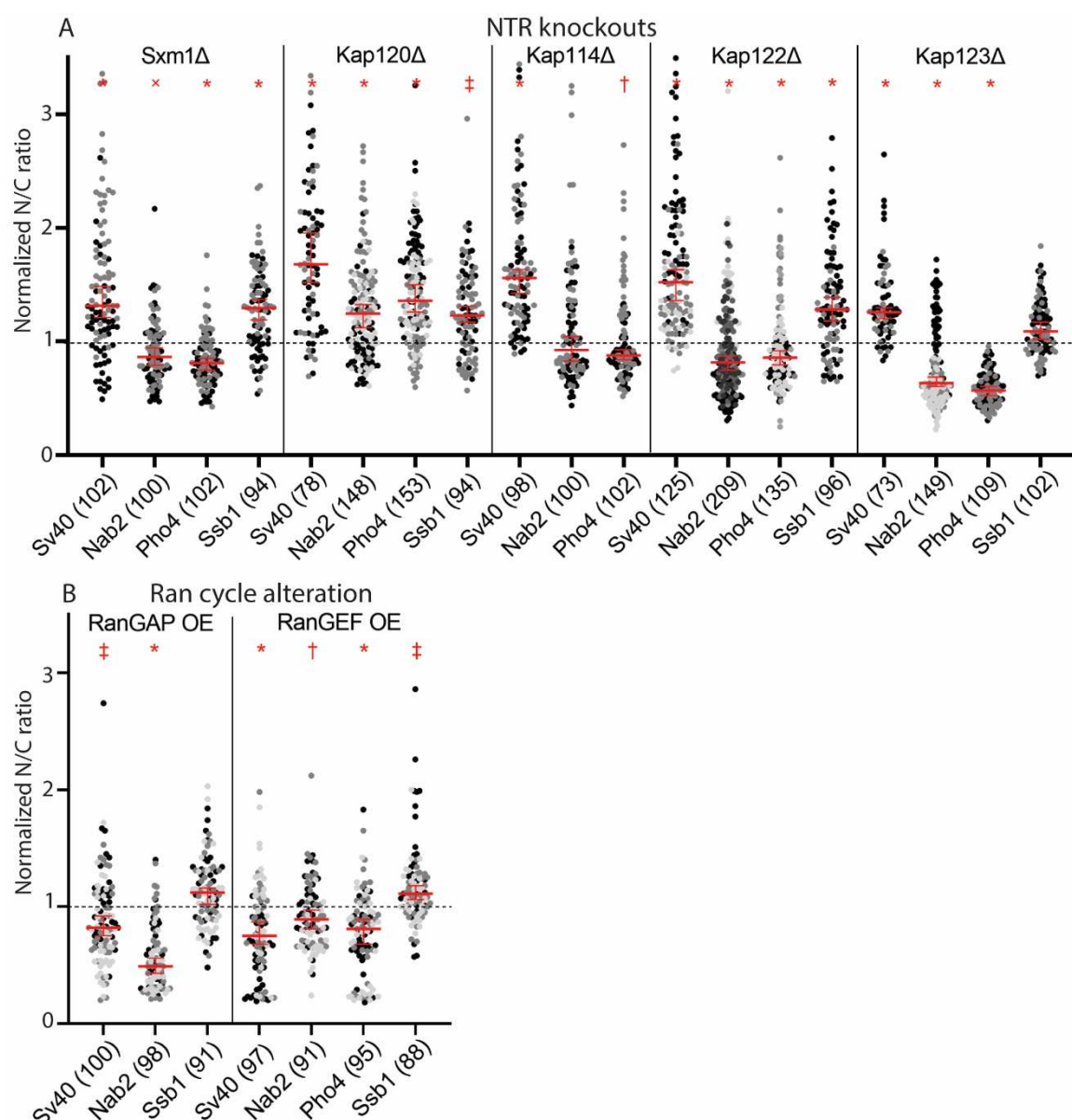
345
346 Next, we aimed to compare the DPR induced transport defects to those induced by making genetic
347 alterations of components of the nucleocytoplasmic transport machinery. First, we used knockouts of
348 five different non-essential NTRs, each one not required for the transport of any of our transport
349 reporters, namely *Sxm1Δ*, *Kap114Δ*, *Kap120Δ*, *Kap122Δ*, and *Kap123Δ*. These five NTRs have different
350 expression levels, cargoes, and localizations (Fig S1B). In general, we find that the knockout of an NTR
351 leads to a greater variability in calculated N/C values of our transport reporters. This is also observed
352 with the environmental stresses and DPR expression, and is possibly a reflection of a derailed cell
353 physiology (compare Fig 4A and Fig 5A, raw values in table S5). Excitingly, the NTR knockouts increase
354 the import of the *NLS_{Sv40}*-reporter, similar to what we saw with polyPR expression. The import of the
355 *NLS_{Nab2}*- and *NLS_{Pho4}*-reporters was decreased in four of the knockout strains, but not in the *Kap114Δ*.
356 *Kap120Δ* increases the import of all three NLS-based reporters. Export in the *Sxm1Δ*, *Kap120Δ*, and
357 *Kap122Δ* strains was decreased, but not significantly altered in *Kap123Δ*. As a second genetic
358 alteration, we overexpressed either RanGAP or RanGEF to see how a misbalance in the Ran cycle would
359 impact transport. We had anticipated that the effect of both overexpressions would be a decrease in
360 transport, since both result in an alteration of the RanGTP gradient. The overexpression of RanGAP
361 and RanGEF does indeed decrease the import and the export of our reporters, but the extent of the
362 effect is variable for the different reporters (Fig 5B, table S5). The *NLS_{Nab2}*-reporter is more susceptible
363 to the overexpression of RanGAP, while export is only impacted when RanGEF is overexpressed.

364
365 In general, we see that the transport of Nab2-containing cargo, as performed by Kap104, is the most
366 variable under the different conditions probed, and an outlier under sublethal heat stress (Fig 4).
367 Export is in general the most stable, although remarkably susceptible to osmotic shock. A comparison
368 between the sizes and directions of the effects on transport induced by the different environmental
369 stressors, mutations and DRPs, shows that they provide unique profiles but, with the exception of the
370 more extreme interventions (24h in water, menadione, ethanol), the effects are of comparable size.
371 The extent of derailment of nuclear transport induced by DPRs is thus to be expected in the same size
372 range as those induced by natural stress conditions such as starvation or osmotic stress. Comparing
373 the NCT phenotypes under these stresses to the data on NCT in polyPR expressing cell, it stands out
374 that whereas most stresses reduce transport, albeit to different extents, NTR knockout leads to an
375 increase in *NLS_{Sv40}*-reporter import, which matches with the effect polyPR expression has.

376
377
378



379
380 **Fig 4. Steady-state N/C ratios of transport reporters under environmental stress conditions.** N/C ratios of GFP-transport
381 reporters in control (A) and indicated stress conditions (B-F), determined in 2-4 independent experiments (grey colours); total
382 number of cells analysed is indicated between brackets, source data 4. Data is normalized to the median control values for
383 each reporter, median and 95% confidence interval are shown in red, Mann-Whitney comparison of each reporter to WT with
384 $\dagger = p\text{-value} < 0.05$, $\ddagger = p\text{-value} < 0.01$, $*$ = $p\text{-value} < 0.0001$. A total of 31 datapoints with normalized N/C above 3.5 are not
385 shown but taken into account in the statistics (respectively 3, 10, 2, 1, 1, 14 points for the datasets in B (Nab2-1h37C, Nab2-
386 10min 46C), C (Ssb1-24h), D (Nab2-NaCl, Ssb1-NaCl), E (Ssb1-Menadione) and F (Ssb1-ethanol). **A)** Wild type BY4741 cells
387 expressing the transport reporters. **B)** Heat shock was performed at 5 minutes or 1 hour at mild (37°C), 5min at severe (42°C),
388 and 10min at sublethal (46°C) temperature stress. **C)** Starvation was performed by growing the yeast cultures to saturation
389 in 20h, or replacing the medium with water. **D)** Osmotic shock was measured immediately after adding 1M NaCl to cells
390 adjusted to the NaPi buffer as control. Normalization of this category is to the osmotic control instead of WT. **E)** Oxidative
391 stress was induced with 4mM H₂O₂, and measured immediately or after 30minutes, or by adding 1,2mM Menadione for
392 40min. **F)** Ethanol stress was performed by adding 15% ethanol to the cultures for 20 minutes.



393
394 **Fig 5. Steady-state N/C ratios of transport reporters in NTR and Ran-cycle mutants. A)** N/C ratios of GFP-transport reporters
395 in WT, and NTR knockout cells, determined in 2-4 independent experiments (grey colours); total number of cells analysed is
396 indicated between brackets, source data 5. Data is normalized to the median WT values for each reporter, median and 95%
397 confidence interval are shown in red, Mann-Whitney comparison of each reporter to WT with † = p-value <0.05, ‡ = p-value
398 <0.01, × = p-value <0.001, * = p-value <0.0001. A total of 8 datapoints with normalized N/C above 3.5 are not shown but taken
399 into account in the statistics (respectively 1,2,2,1,1 and 5 points for the datasets SV40-Sxm1Δ, Nab2-Kap120Δ, Pho4-
400 Kap120Δ, Nab2-Kap114Δ, SV40-Kap122Δ, Nab2-Kap122Δ). **B)** As in A but now for cells overexpressing RanGAP or RanGEF.

401
402 **Similarities between transport effects in C9-ALS models and stress conditions**
403 To further investigate which stress-induced transport phenotype shows similarity with the transport
404 phenotypes observed in the C9ALS model, we performed clustering analysis of the transport datasets.
405 We first performed a Principal Component Analysis to show how similar or dissimilar the stresses are,
406 and which component (i.e. transport reporter) mainly influences this (dis)similarity. This is represented
407 by a biplot (Fig 6A), which shows that the phenotypes for the strong effectors menadione, ethanol,
408 and water shock, are clearly very different from the other stresses. It does not allow analysing the
409 similarities and differences in the conditions inducing more subtle changes. However, when clustered
410 in 5 categories, as by the k-means clustering analysis, we find more meaningful clustering, as e.g. now
411 the conditions that increase classical transport become a separate category. These categories are

412 represented in the biplot with different colours of the labels and in the heatmap in separate blocks (Fig
413 6A/B). The first cluster includes menadione induced ROS and is characterized by a strong defect for the
414 import reporters reducing the N/C ratios to 1 (Fig 6B & table S4). The second cluster of water starvation
415 and ethanol includes basically the two ‘outliers’ in the biplot, where the common factor is the
416 reduction of the classical import route, but to a smaller degree than we saw for menadione treatment.
417 The next three categories are the biologically more relevant ones. Cluster 3 includes PR expression,
418 and the NTR knockout strains Sxm1Δ, Kap122Δ, and Kap123Δ; cluster 4 includes Kap120Δ, the osmotic
419 shock control, peroxide after 30min, mild heat shock after 1h, and 10min sublethal 46°C heat shock,
420 and cluster 5 includes peroxide stress, phosphate buffer, 5min mild and severe heat shock (37°C and
421 42°C), RanGEF overexpression, GA expression, saturated growth and osmotic shock. Kap114Δ and
422 RanGAP OE were not included in the PCA, because one category of transport data was lacking.
423 However, the similarities in the pattern of the effects, as shown in the heatmap and the bar graphs,
424 allowed us to manually add Kap114Δ with the other NTR knockouts in group 3, and RanGAP OE with
425 group 5.

426 We will describe the characteristics of cluster 3-5 in more detail: Cluster three is dictated by the
427 improved import of the Sv40-reporter, together with reduced Nab2- and Pho4-reporter import. The
428 effects on export are dissimilar, as they are increased in polyPR-expressing cells, and reduced in the
429 NTR knockout strains. The average pattern of changes in transport is shown in figure 6C.

430 The fourth cluster gathers adaptations to environmental stresses and is mainly determined by the
431 increase of Nab2- and Pho4-reporter import, and in part by the increase of Sv40-reporter import and
432 reduced export. Kap120Δ shows the strongest improvement of import. The conditions probed reflect
433 adapted cell states where the transport returns to wild type situation. Cells placed in NaPi buffer show
434 reduced import in the first ~10minutes, but later adapt to this buffer (NaPi shock compared to osmotic
435 control in table S4). Also, peroxide initially triggers a response (see cluster 5) but peroxide readily
436 degrades and is no longer present after 30 minutes, when cells have adapted.

437 The fifth cluster has the smallest changes in NCT and is defined by reduced import, but less strong than
438 in the first two clusters, as well as reduced export. The common denominator for this category is the
439 alteration of energy maintenance conditions: RanGAP and RanGEF overexpression affect the Ran cycle
440 directly; peroxide stress impacts mitochondria; saturated growth limits glucose availability and
441 imposes mild oxidative stress linking back to mitochondrial stress; the heat shock is related to energy
442 generation⁸³ and the heat shock response regulates glycolysis as one of the key processes⁸⁴; and
443 osmotic shock is related to metabolic changes⁸⁵.

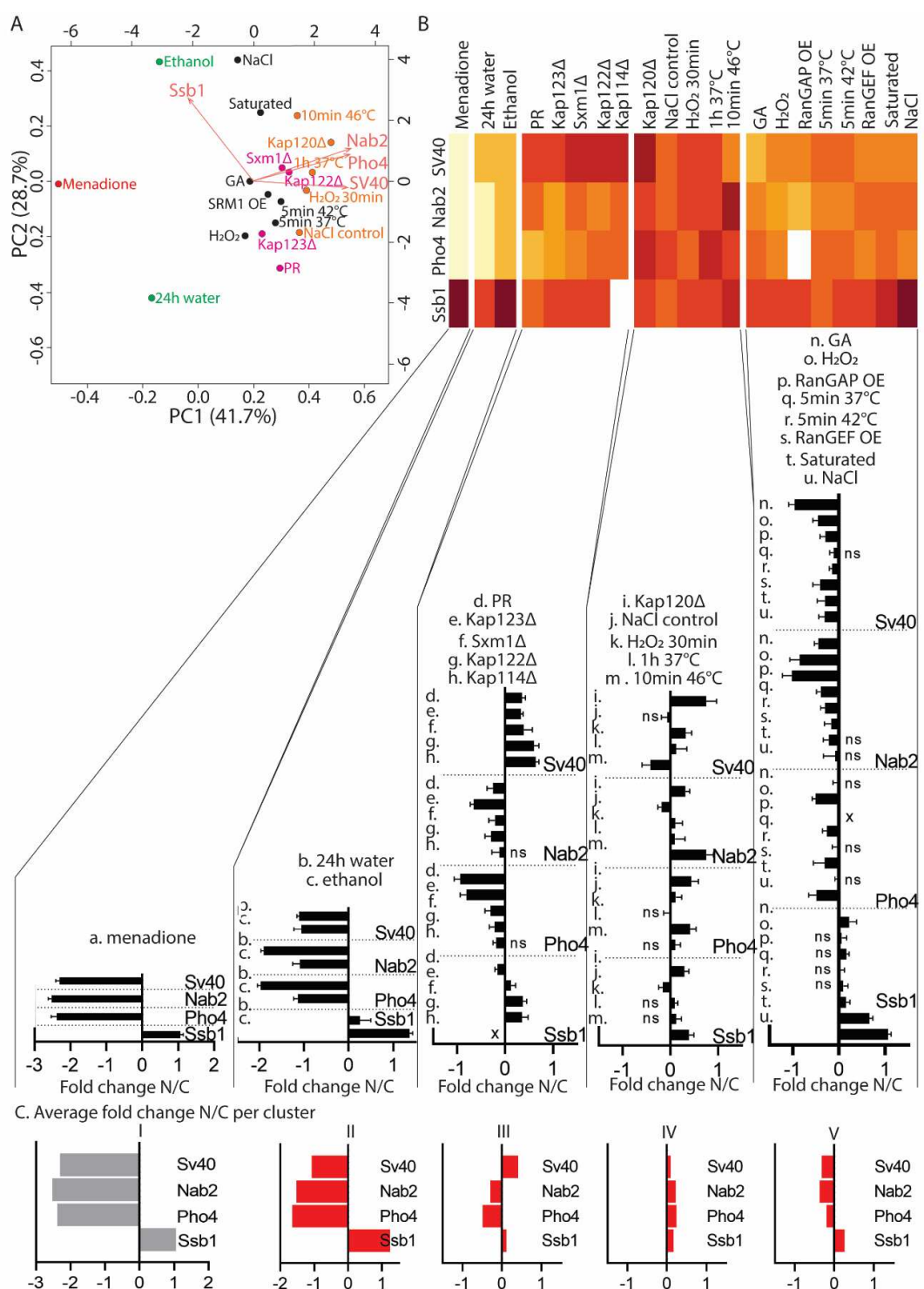
444

445 In short, we see that different stresses have variable effects on transport, and we can distinguish
446 categories which overlap with the effect of polyPR and polyGA expression. In this case, it allows us to
447 cluster polyPR expression with alterations in NTR levels, and polyGA expression with stresses that
448 affect energy maintenance. If we consider that changes in NCT for the four import routes and the
449 export route may serve as a fingerprint reporting on cell physiology, then we may infer that polyPR
450 and polyGA expression impact the maintenance of, respectively, NTR and energy levels.

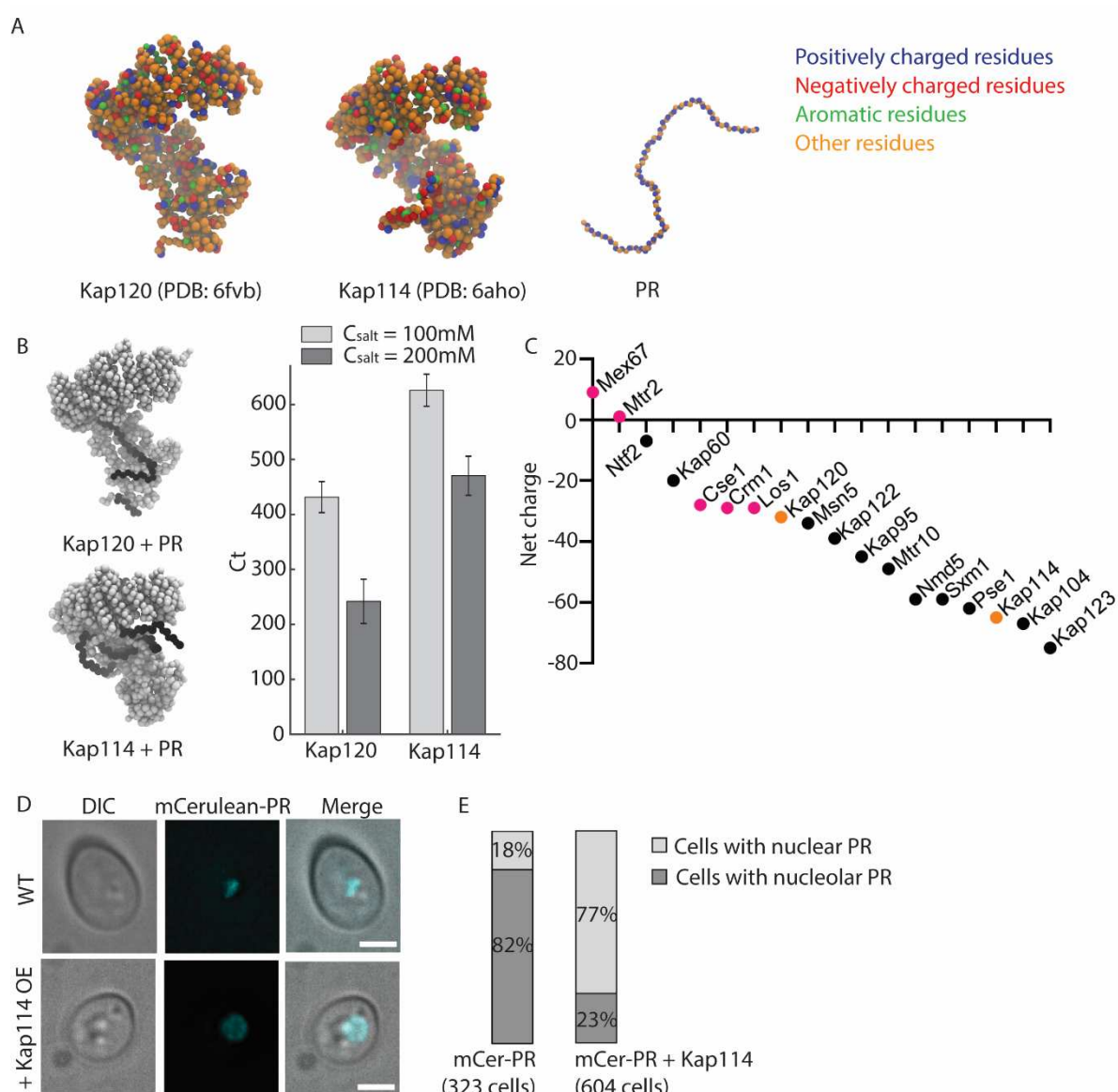
451

452 Here we specifically address a possible cellular mechanism (that has also previously been
453 proposed^{51,55}), namely, that polyPR binds to NTRs which decreases their availability for transport. In
454 cells, NTR levels are finely tuned, the majority of NTR knockouts are inviable, and overexpression of
455 NTRs leads to toxicity (Fig S2). The distinct behaviour of Kap120Δ provided an entry point into the
456 question whether polyPR may alter NCT by binding NTRs. As shown in figure 5A, the transport profile
457 of Kap120Δ is different from the other four: while Sxm1Δ, Kap114Δ, Kap122Δ, and Kap123Δ show
458 respectively an increase, a decrease, a decrease and an increase in the N/C ratio reporting on the
459 transport of NLS_{Sv40}-, NLS_{Nab2}, NLS_{Pho4}, and NES_{Ssb1}-GFP reporters, in Kap120Δ cells all reporters have an
460 increased N/C ratio. Previously it was shown that polyPR can bind importins^{51,55} and hence we
461 investigated the possibility that the distinct behaviour of transport in Nup120Δ cells is related to a
462 difference in its capacity to bind polyPR.

463 To compare the capacity of the NTRs Kap120 and Kap114 to bind to polyPR, we performed coarse-
464 grained molecular dynamics simulations. For this purpose, we developed residue-scale models of
465 Kap120 and Kap114 for which the crystal structures of unbound state are known (PDB codes 6fvb and
466 6aho, respectively). The coarse-grained models preserve the overall structure of Kap120 and Kap114
467 (Fig 7A). Additionally, the distribution of charged and aromatic residues that are relevant for the
468 interaction of arginine-rich DPRs with NTRs are included in the model. For polyPR, we used a coarse-
469 grained model that has already been applied to study the phase separation of polyPR with negatively-
470 charged proteins⁸⁶. More details about the coarse-grained force field are provided in the Materials and
471 Methods section. We observed direct binding of Kap120 and Kap114 to PR₅₀ at monovalent salt
472 concentrations of 200mM and 100mM. To quantify the binding, we calculated the time-averaged
473 number of contacts C_t between polyPR and the NTRs (Fig 7B). As can be seen, reduction of the salt
474 concentration, which reduces screening effects, increases the number of contacts, thus showing the
475 important role of electrostatic interactions in polyPR-NTR binding. For C_{salt} = 200mM, a condition
476 similar to previous *in vitro* experiments⁵⁵, we observe a significantly lower number of contacts (around
477 2 times lower) for Kap120 compared to Kap114. This difference in binding behavior can be related to
478 a difference in the net charge of these two NTRs.
479 When comparing the net charge of all yeast NTRs by subtracting the positively charged residues
480 (Arg/Lys) from the negatively charged residues (Asn/Glu), it is striking that Kap114 (in orange in Fig 7C)
481 and Sxm1, and Kap123 from the transport cluster 3, are similarly strongly negatively charged with net
482 negative charges of 65, 59 and 75, respectively. The exportins are on the left side of the graph, showing
483 RNA exportins Mex67-Mtr2 with net positive charges, and Cse1, Crm1, and Los1 with a net negative
484 charge of 28 and 29, respectively (in magenta in Fig 7C). Kap120, from cluster 4 is present on the left
485 side of this graph as well with a net charge of -32 (in orange in Fig 7C).
486 The direct binding of polyPR and Kap114 predicted by the simulations made us wonder why Kap114-
487 GFP and polyPR were not observed to colocalize in cells (Fig S1B). We tested the possibility that the
488 normal cellular levels of Kap114 may be too low to support stable association with polyPR. We thus
489 overexpressed Kap114 and followed the subcellular localization of mCerulean-PR. We indeed see that
490 overexpression of Kap114 relocalized mCerulean-PR from the nucleolus. Specifically, without
491 overexpression of Kap114, mCerulean-PR is nucleolar in 82% of cells, but with overexpression of
492 Kap114, mCerulean-PR has a nuclear diffuse localization in 77% of cells (Fig 7D/E).
493
494 We conclude that the distinct transport profile of Kap120Δ cells compared to the transport profiles of
495 the other NTR knockouts and cells expressing polyPR (Fig 6), and the prediction of ionic interaction
496 between polyPR and negatively charged NTRs (Fig 7), can be taken as an indication that the mechanism
497 through which polyPR derails NCT is by depleting the cells of functional NTRs.
498
499
500



501
502 **Fig 6. Similarities and differences in nuclear transport defects. A)** K-means clustering leads to five categories, shown here on
503 a biplot based on the median values of the four transport reporters, each group in one colour. **B)** The five categories as shown
504 by their fold change for the different transport reporters. Cluster 1) the strongest change is seen for menadione stress and
505 24h water stress; these strongly reduce import and export, menadione reduces import to the maximal extent of reaching N/C
506 ratios of 1. Cluster 2) 0.5h water and ethanol stress strongly reduce export, with ethanol reducing export to N/C ratios of 1,
507 and reduce import less strong than group 1. Cluster 3) PR expression, and the NTR knockout strains Kap123Δ, Sxm1Δ,
508 Kap122Δ, and Kap114Δ show an increase in import of the SV40 reporter, and reduced import of the other reporters. Export
509 is reduced for the NTR knockouts, but increases for the PR expressing strain. Cluster 4) Kap120Δ, the osmotic shock control,
510 peroxide after 30min, mild heat shock after 1h, and 10min sublethal 46°C heat shock are grouped based on a slight increase
511 in import, and small decrease in export. Cluster 5) peroxide stress, RanGAP overexpression, phosphate buffer, 5min mild and
512 severe heat shock (37°C and 42°C), RanGEF overexpression, GA expression, saturated growth and osmotic shock are
513 categorized by a general decrease of import, while export is unaltered or reduced. **C)** Shows the average N/C fold change of
514 the intervention in the cluster.



515
516 **Fig 7. Investigating electrostatic interactions of Kap114 and Kap120 with polyPR.** **A**) Schematic depiction of residue-scale
517 coarse-grained models of Kap120, Kap114, and PR₅₀ with the different bead types highlighted. **B**) PR₅₀ time-averaged number
518 of contacts Ct with Kap120 and Kap114 calculated at two different monovalent salt concentrations $C_{salt} = 100\text{mM}$ and 200mM.
519 Two snapshots for PR₅₀-Kap120 and PR₅₀-Kap114 binding at $C_{salt} = 200\text{mM}$ are shown on the left, with polyPR depicted in
520 black and NTRs in grey. Simulations are performed for 2.5μs and the last 2μs are used for the contact analysis. **C**) Overview
521 of the net charge of each NTR, by subtracting the positively charged residues (Arg/Lys) from the negatively charged residues
522 (Asn/Glu), source data 6. Colour-coded are the exportins in magenta, and the Kap120 and Kap114 in orange. **D**) Subcellular
523 localization of mCerulean-PR. mCerulean-PR localizes to the nucleus, with a preference for the nucleolus (top panels), but
524 when Kap114 is co-expressed mCerulean-PR becomes more diffusely nuclear. **E**) Frequency of nucleolar (D top panel) or
525 nuclear diffuse (D bottom panel) mCerulean-PR signal observed in cells expressing mCerulean-PR or co-expressing
526 mCerulean-PR and Kap114. Total numbers of cells counted indicated.

527
528
529
530
531
532
533
534
535

536 Discussion

537 In this study we comprehensively analyze the transport defects arising from expression of C9ALS
538 associated DPRs and compare them to those occurring in several stress conditions and mutants. The
539 systematic quantitative assessment of 100 different transport readouts from four transport reporters
540 revealed, first of all, that DPR expression impacts transport about as much as exposure to common
541 environmental stresses. Projecting the data from our four transport receptors to the whole proteome,
542 our data predicts a chronic global mislocalization of many proteins, which could have severe effects on
543 cellular viability. A comparison of the specific patterns of alterations in transport related to the
544 expression of polyPR and polyGA, to those obtained when cells were exposed to different stress
545 situations, revealed striking similarities. The transport phenotype of polyPR expressing cells clusters
546 with those measured in four NTR deletion mutants, while the transport phenotype of polyGA
547 expressing cells clusters with stresses that affect energy maintenance. If we consider that changes in
548 NCT may serve as a fingerprint reporting on cell physiology, then we may infer that the cellular
549 mechanisms compromised by polyPR or polyGA expression are related to the maintenance of,
550 respectively, NTR availability and energy levels.

551

552 Our study thoroughly characterizes the yeast model expressing PR₅₀ or GA₅₀, in terms of toxicity and
553 changes of the NCT machinery. It recapitulates the toxicity and localization of the DPRs as reported in
554 other models, where PR₅₀ is toxic and localized in the nucleolus and GA₅₀ is often not toxic and forms
555 aggregates in the cytosol^{35–39,48,59,60,63–65} (and reviewed in⁴⁰). Our analysis of the abundance and
556 localization of the components of the nuclear transport machinery, including NPC components, almost
557 all NTRs, and the components of the Ran gradient, shows that expression of polyGA and polyPR does
558 not induce significant changes. Our data does not support blocking of NPCs, nor does it show
559 prominent colocalization of DPRs with NTRs or the NPC as previously reported^{52,87,88}. At the same time,
560 we do find that the expression of both DPRs impact the transport by different NTRs (Crm1,
561 Kap60/Kap95, Kap104, and Kap121/Pse1) to varying degrees and directions. Specifically, polyPR
562 increases the transport by Kap60/95, and Crm1, but decreases transport of the other two import
563 routes. In contrast, polyGA reduces transport by Kap60/95 and Crm1, but does not impact Pse1
564 transport.

565

566 We found that the transport phenotype of polyPR expressing cells clusters with those measured in four
567 NTR deletion mutants. We propose that the similarity between the NCT profiles measured upon the
568 removal of one NTR -as in the knockouts- and the polyPR expressing strains may mechanistically be
569 explained by the electrostatic interaction of polyPR with NTRs, as shown in our coarse-grained
570 molecular dynamics simulations. Such direct biding of polyPR to NTRs is in line with previous
571 reports^{51,55}. The binding of polyPR to NTRs may leave these NTRs unsuited to bind their cargo and/or
572 the FG-Nups of the NPC, thereby compromising transport. Following this logic, both polyPR expression
573 and deletion of the more negatively charged NTRs, Sxm1, Kap122, and Kap123, result in a reduction of
574 the pool of functional NTRs, and thus in similar transport defects.

575

576 The similarity in NCT phenotypes of polyGA expressing cells and diverse environmental challenges
577 (glucose deprivation, oxidative stress, and heat stress) to which the cells have evolved adaptive
578 mechanisms might explain why polyGA expression is not toxic. It may also suggest that the transport
579 defects arise secondary to the stress associated with polyGA expression. It would be interesting to
580 compare these transport phenotypes to those obtained with the expression of other non-toxic
581 aggregation prone proteins; if similar this may reflect the profile of a cell in which protein homeostasis
582 is challenged.

583

584 How do we value our data towards the understanding of C9ALS? Specifically related to the
585 multifactorial nature of C9ALS, where the G₄C₂ sequence of the genome, the RNAs that are transcribed
586 as well as the 5 different DPRs all exert their effects, a direct translation for the reductionists approach

587 taken here is not possible. In addition, the yeast model is obviously very distant from humans.
588 However, due to the conservation of basic biology, including the NCT system, we can infer that our
589 data suggest that also in patients there will be a global impact on the kinetics of transport.
590 Quantitatively, the impact on transport is expected to be in the same order as those measured in
591 different physiologically relevant stresses including ageing. The quantitatively modest effects on NCT
592 may be the explanation for the diverse outcomes of transport studies in the literature (reviewed in⁴⁰).
593 As to the question of causality, our data supports that some aspects of the C9orf72 pathology are
594 indirect while other are related to direct interactions with the NCT machinery. Whether such direct
595 interactions with the NCT provide opportunities for future interventions should be investigated more
596 thoroughly and preferably these studies should go hand-in-hand with studies investigating the
597 robustness of NCT under stress and ageing.
598

599 Materials and methods

600 Strains and growth conditions

601 All *Saccharomyces cerevisiae* strains used in this study have the BY4741 genotype, and are listed in
602 Table 4. For the fluorophore-tagging of DPRs mCerulean3 was PCR amplified from CrGE2 (Crowding
603 sensor⁸⁹) and inserted between GAL1 promotor and PR₅₀ sequence via BamHI/PstI sites. The ATP
604 sensor was constructed by integrating a synthetic pTEF1-his6-ymEGFPΔ11-B.subtilis ε construct
605 (GeneArt, ThermoFischer, as based on⁷⁰) into a pRS303-ymScarletI vector using Spel/Ncol sites. Apart
606 from the strains in Fig 1C/D, all DPR containing strains were transformed with pRS416-PR₅₀/GA₅₀. Fig
607 1C/D was made with the mCerulean-tagged DPRs. GFP-tagged strains were taken from the 4000-GFP
608 yeast library (Thermofisher), while knockout strains were taken from the Yeast Knockout Collection
609 (Invitrogen).

610 For expression of DPRs and transport reporter proteins, cells were grown at 30°C, with shaking at 200
611 RPM using the appropriate Synthetic Dropout medium supplemented with 2% glucose in overnight
612 culture. The next day cultures were diluted 1:10 in SD medium supplemented with 2% D-raffinose, and
613 again for an overnight culture. Expression of DPRs and transport reporter proteins was induced with
614 0.1% galactose 3h prior to the start of an experiment, while the cultures had an OD_{600nm} between 0.6-
615 0.9. For the different stress conditions the transport reporters were induced with 0.1% galactose for
616 1h.
617

618 Spot assay

619 Cells were grown overnight in 2% glucose containing medium, diluted the next day 1:10 in 3ml 2%
620 raffinose medium. At the end of the day cells were diluted to obtain a culture of OD_{600nm} ~0.3 the
621 following morning. This culture was used to dilute cells in sterilized water to obtain 10⁴-10⁶ cell/ml
622 densities, and then 5µl was spotted on the appropriate YPD or YPGal plates.
623

624 Microscopy

625 Microscopy was performed at 30°C on a Delta Vision Deconvolution Microscope (Applied Precision),
626 using InsightSSITM Solid State Illumination of 435 and 525 nm, an Olympus UPLS Apo 40x or 100x oil
627 objective with 1.4NA and softWoRx software (GE lifesciences). Detection was done with a CoolSNAP
628 HQ2 or PCO-edge sCMOS camera.
629

630 Microfluidic devices

631 To determine division times for the PR₅₀/GA₅₀ expressing strains, an ALCATRAS chip was used as
632 previously detailed⁶². DIC images of cells were taken every 20 min. to follow all divisions of each cell.
633 The efflux assay was performed in the CellASIC Onix microfluidic perfusion system (Merck Millipore).
634 Cells were loaded 3 times 5 sec. at 8psi or 5psi for smaller cells, medium was run at 2psi to flush out
635 free cells. Medium was exchanged for the appropriate synthetic dropout medium supplemented with
636 10 mM sodium azide and 10 mM 2-deoxy-D-glucose⁹⁰, additionally ponceau S was used to allow
637 fluorescence in the A594 channel to determine when the poison front hit the cells. The addition of

638 sodium azide and 2-deoxyglucose depletes the cell of energy and destroys the Ran-GTP/GDP gradient
639 thus abolishing active transport of reporter proteins. We measured the net efflux of reporter proteins
640 by imaging the cells every 2,5 millisecond for a period of 20 seconds in the FITC channel starting 5
641 seconds after the poison front.

642

643 **Data analysis of N/C ratios and efflux rates**

644 Microscopy data was quantified with open source software Fiji (<https://imagej.net/Welcome>⁹¹).
645 Fluorescent intensity measurements were corrected for background fluorescence. To quantify the
646 nuclear localization (N/C ratio) of the reporters, the average fluorescence intensity at the nucleus and
647 cytosol were measured. The nuclear area was determined using live Hoechst33342 stain (NucBlue Live
648 Cell Stain Ready Probes, Invitrogen) or using the signal of the GFP-reporters in case of the poison assay.
649 A section in the cytosol devoid of vacuoles was selected for determining the average fluorescence
650 intensity in the cytosol. Leak rates were determined by linear regression lines in GraphPad Prism
651 (version 8.3.0). Cells with linear regression lines with standard deviation of the residuals (Sy.x) above
652 0.03 were excluded from the analysis. Statistical parameters including the definitions and exact values
653 of N, distributions and deviations are reported in the figures and corresponding figure legends. Each
654 single cell counts as a biological replicate, and grey colours in the figures 3,4, and 5 are different
655 cultures. Significance of changes were determined with a Mann-Whitney test, since not all measured
656 conditions were normally distributed.

657

658 **Stress interventions**

659 All stress interventions were performed after induction of the transport reporters with 0.1% galactose
660 for 1h, and additionally incubated for 5 minutes with NucBlue (NucBlue Live Cell Stain Ready Probes,
661 Invitrogen), to allow for determination of the nuclear area.

662 Heat shock was performed after growing the cells as previously stated, then harvesting 1.5ml cells and
663 replacing the medium with preheated medium at the appropriate (37°C/42°C/46°C) temperature. Next
664 the culture was maintained at this temperature for 5 or 10 minutes (as indicated) in a water bath, after
665 which cells were immediately imaged.

666 Starvation was performed either by growing the culture to saturation in medium with 2% raffinose
667 over 20 hours, after which the reporters were induced with 0.1% galactose for 1h. For the water
668 starvation experiment, we followed the method as previously described⁹². In short, GFP-reporter
669 strains were grown in SD medium supplemented with 2% glucose and grown overnight. The next day,
670 cells were diluted in Sgal medium with 4% D-galactose and grown to an OD_{600nm} between 0.6 and 0.9.
671 Then cells were harvested and resuspended in water, and maintained shaking at 30°C. Samples were
672 taken from the galactose culture at t=0, and from the water culture after 30min, followed by a sample
673 after 24hr.

674 Osmotic shock was performed as described previously⁸². In short, 1.5ml of cells was harvested after
675 induction of the transport reporters, and resuspending in either 100µl low osmolality buffer (50mM
676 NaPi, pH 7), or high osmolality buffer (50mM NaPi, 1M NaCl) to induce osmotic upshift.

677 Oxidative stress was performed by adding 4mM H₂O₂ (Sigma-Aldrich) to 1.5ml of induced cells and
678 imaging directly, or by adding 1.2mM menadione (Sigma-Aldrich) for 40 minutes overlapping with the
679 galactose inducing.

680 15% (v/v) ethanol was added during the last 20minutes of galactose induction.

681

682 **Cluster analysis of interventions**

683 For each intervention, the median fold change compared to wild type, on log2 scale, was used in a
684 Principal Component Analysis (prcomp, centered and scaled; R studio version 1.4.1717). This data was
685 used for the standard function of the biplot and the heatmap of R. The clustering was performed with
686 the data.kmeans function (5 clusters, iter.max = 10, n = 25).

687

688

689

690 **Proteomics sample preparation**

691 10ml cultures of wild type, PR₅₀- and GA₅₀-repeat expressing cells were grown as described. Cells were
692 harvested, washed twice in PBS, and lysated by shaking with glass beads according to the yeast
693 protocol in the FastPrep machine (MpBio). Yeast lysate samples were mixed with LDS loading buffer
694 (NuPAGE) at a concentration of 10 ug total protein in a total volume of 20 μ L. The sample was run
695 briefly into a precast 4-12% Bis-Tris gels (Westburg, ran for maximally 5 min at 100 V). The band
696 containing all proteins was visualized with Biosafe Coomassie G-250 stain (Biorad) and excised from
697 gel. Small pieces were washed subsequently with 30% and 50% v/v acetonitrile in 100 mM ammonium
698 bicarbonate (dissolved in milliQ-H₂O), each incubated at RT for 30 min while mixing (500 rpm) and
699 lastly with 100% acetonitrile for 5 min, before drying the gel pieces at 37 °C. The proteins were reduced
700 with 30 μ L 10 mM dithiothreitol (in 100 mM ammonium bicarbonate dissolved in milliQ-H₂O, 30 min,
701 55 °C) and alkylated with 30 μ L 55 mM iodoacetamide (in 100 mM ammonium bicarbonate dissolved
702 in milliQ-H₂O, 30 min, in the dark at RT). The gel pieces were washed with 100% acetonitrile for 30 min
703 while mixing (500 rpm) and dried in at 37 °C before overnight digestion with 30 μ L trypsin (1:100 g/g,
704 sequencing grade modified trypsin V5111, Promega) at 37 °C. The next day, the peptides were eluted
705 from the gel pieces with 30 μ L 75% v/v acetonitrile plus 5% v/v formic acid (incubation 20 min at RT,
706 mixing 500 rpm). The elution fraction was diluted with 900 μ L 0.1% v/v formic acid for cleanup with a
707 C18-SPE column (SPE C18-Aq 50 mg/1mL, Gracepure). This column was conditioned with 2x1 mL
708 acetonitrile plus 0.1% v/v formic acid, and re-equilibrated with 2x1 mL 0.1% v/v formic acid before
709 application of the samples. The bound peptides were washed with 2x1mL 0.1% v/v formic acid and
710 eluted with 2x0.4 mL 50% v/v acetonitrile plus 0.1% v/v formic acid. The eluted fractions were dried
711 under vacuum and resuspended in 0.1% v/v formic acid to a final concentration of around 1 μ g/ μ L total
712 protein starting material.

713

714 **Targeted proteomics analyses**

715 Selected reaction monitoring (SRM) analyses were performed on a triple quadrupole mass
716 spectrometer with a nano-electrospray ion source (TSQ Vantage, Thermo Scientific) for the peptides
717 listed in Table 2, for which isotopically labeled peptides were derived from generated QconCATs (these
718 QconCATs were kindly provided by Prof. R. Beynon, University of Liverpool UK). Chromatographic
719 separation of the peptides was performed by liquid chromatography on a nano-UHPLC system
720 (Ultimate UHPLC focused, Thermo Scientific) using a nano column Acclaim PepMapC100 C18, 75 μ m x
721 50 cm, 2 μ m, 100 Å, Thermo Scientific). Samples were injected at a concentration of 1 μ g protein and
722 an amount of isotopically-labeled standards optimized for the chosen application using the μ L-pickup
723 system using 0.1% v/v formic acid as a transport liquid from a cooled autosampler (5 °C) and loaded
724 onto a trap column (μ Precolumn cartridge, Acclaim PepMap100 C18, 5 μ m, 100 Å, 300 μ m id, 5 mm
725 Thermo Scientific). Peptides were separated on the nano-LC column using a linear gradient from 3-60
726 % v/v acetonitrile plus 0.1% v/v formic acid in 100 minutes at a flowrate of 300 nL/min. The mass
727 spectrometer was operated in the positive mode at a spray voltage of 1500 V, a capillary temperature
728 of 270 °C, a half maximum peak width of 0.7 for Q1 and Q3, a collision gas pressure of 1.2 mTorr and
729 a cycle time of 1.2 ms. Optimal collision energies (CE) were predicted using the following linear
730 regressions: CE = 0.03*m/z precursor ion + 2.905 for doubly charged precursor ions, and CE=0.03*m/z
731 precursor ion +2.467 for triply charged precursor ions. For each of the peptides, the optimal precursor
732 charge and three optimal transitions were selected after screening with the QconCAT peptides. The
733 measurements were scheduled in windows of 5 minutes around the pre-determined retention time.
734 For NTR, Nup, and Ran cycle component abundances were calculated as amount compared to total
735 protein amounts. Then the average of three runs, one being a technical and one a biological replicate,
736 each in triplicate, was used to normalize PR- and GA-expressing cell abundances to WT amounts
737 (Source data 1, for biological and technical replicates).

738

739

740 **Discovery-based proteomics analyses**

741 Discovery mass spectrometric analyses were performed on an orbitrap mass spectrometer with a
742 nano-electrospray source (Orbitrap Q Exactive Plus, Thermo Scientific). Chromatographic separation
743 of the peptides was performed by liquid chromatography on a nano-HPLC system (Ultimate 3000,
744 Thermo Scientific) using a nano-LC column (Acclaim PepMapC100 C18, 75 μ m x 50 cm, 2 μ m, 100 \AA ,
745 Thermo Scientific). In general, an equivalent of 1 μ g total protein starting material was injected using
746 the μ L-pickup method with 0.1% v/v formic acid as a transport liquid from a cooled autosampler (5 $^{\circ}$ C)
747 and loaded onto a trap column (μ Precolumn cartridge, Acclaim PepMap100 C18, 5 μ m, 100 \AA , 300
748 μ m x 5 mm, Thermo Scientific). Peptides were separated on the nano-LC column using a linear gradient
749 from 2-45% v/v acetonitrile plus 0.1% v/v formic acid in 85 min at a flowrate of 300 nL/min. The mass
750 spectrometer was operated in the positive mode in a data-dependent manner, with automatic
751 switching between MS and MS/MS scan using a top-15 method. MS spectra were acquired at a
752 resolution of 70.000 with a AGC target of 3e⁶ ions or a maximum integration time of 50 ms at a scan
753 range of 300 to 1650 m/z. Peptide fragmentation was performed with higher energy collision
754 dissociation (HCD) with the energy set to 28 NCE. The intensity threshold for ions selection was set at
755 2.0e⁴ with a charge exclusion of 1≤ and ≥6. The MS/MS spectra were acquired at a resolution of 17.500,
756 with a target value of 1e⁵ ions or maximum integration time of 50 ms and the dynamic exclusion set to
757 20 sec.

758

759 LC-MS raw data were processed with MaxQuant (version 1.5.2.8⁹³). Peptide and protein identification
760 was carried out with Andromeda against a yeast SwissProt database (www.uniprot.org, 6721 entries,
761 downloaded on June 2020). For peptide identification two miss cleavages were allowed, a
762 carbamidomethylation on cysteine residues as a static modification and an oxidation of methionine
763 residues and acetylation of protein N-termini as variable modifications. Peptides and proteins were
764 identified with an FDR of 1%. For a protein identification at least one unique peptide had to be detected
765 and the match between runs option was enabled. Proteins were quantified with the MaxLFQ
766 algorithm⁹⁴ considering only unique peptides and a minimum ratio count of one. Results were exported
767 as tab-separated *.txt for further data analysis.

768 For cargo abundances, only one exploratory MS run in triplicate was performed, therefore only LFQ
769 intensities were averaged over one set of triplicates, and compared between WT, PR-, and GA-
770 expressing cells (Source data 3).

771

772

773

774

775

776

777

778

779

780

781

782

783

784

785

786

787

788

789

790

791

Table 2. SRM mass spectrometry peptides in this study

CRM1	SDLTLVQILK	NUP1	SGEDTNVGLPILK
CSE1	YNAISGNTFLNTILPQLTQENQVK	NUP2	FSLPFEQK YEPLAPGNDNLIK
KAP60	IIEVTLDALENILK AVGNIVTGNDLQTQVVINAGVLPALR	MLP1	SFDGDVVK VTVSFDELK
KAP95	TNALTALVSIEPR LAALNALADSLIFIK	POM152	SSSGGFNPFTSPSPNK ACAANVDQISFLEPINLK
KAP104	FISNPNFSPVIR		NQILVSITDAPK
KAP114	TLENILVSQEIPELILAR ALANVALQHEASLESR	POM34 POM33	NVFGTLQR NEPLQTQDAAATK
KAP120	INTEFLNENLITR VPLILPLIVR	NDC1 NIC96	LTAYQELAYR IVFQFNNSR
KAP122	SDLNSYTDLLR		YSLEDFQNIIISYGPSR
KAP123	VYGENFAPFLK	NUP82	LSALPIFQASLSASQSPR
LOS1	VSLNVLCNFIK		AQTLGVSIHNR
MEX67	LNPVQLELLNK	NUP192	SNFILEVFGTIIPK
MSN5	GLPTVVQSFVK		GGASALIENNLFK
MTR2	LAQFVQLFNPNNCR	NUP188	NSLLLDSTPEEVSCK
NMD5	NLEQSFYPAAEFLK AVTAEDNSLDDLR	NUP170	FALFAESHDVQLK ASTIISPGIFFSAVIK
NTF2	SQLGNLYR	NUP157	LYVSAPDYGILK
PSE1	ILGDDFVPLLPVIPPLLITAK		NAPSPDVGSVGQESFLSSISNTLIR
SXM1	VSTNDELGLDSK	ASM4	LTYNSPSSALR
YRA1	VLLSYNER	NUP133	IFNTNSSVVSLR
YRA2	EFGSPIFSK		TVVINSVDVFPVIFK
YRB2	VILNIQLVK SGEESEECIYQVNAK	NUP120	LQILNVNDESFK SLVDLQSEHLDIVTK
		NUP85	SSNLYETIIEADK
NUP159	INHTEELLNILK ALSENPFTSANTSGFTFLK	NUP84 SEH1	GTEASNDIIDKPYLLR LACLGNDGILR
NUP145	LSSILFDPVSYPYK LLSNNPVQNNELK		LYDALEPSDLR
NUP116	NFSFEELR	SEC13	LIDTLTGHEGPVWR FGTILASCYDGK
NUP100	NNYYISPSIETLGNK		
NSP1	TTNIDINNEDENIQLIK	GSP1	LVLVGDGGTGK
NUP57	NQVQTENVAQAR IVEILTNQQR	RNA1	LDLSGNTIGTEASEALAK NLEILDLDQDNTFTK
GLE2	VASGGCDNALK	SRM1	THASHIINAQEDYK
GLE1	IQNELTQLINDTK		SIAAGEHHSLISQDGDLYSCGR
NUP60	SVVVSAVGEAR NVEPTENAYK		

792 **Coarse-grained model**

793 We use a modified version of the implicit solvent, coarse-grained one-bead-per-amino acid (1BPA)
794 model developed earlier⁹⁵. The coarse-grained models of Kap120 (PDB:6fvb) and Kap114 (PDB:6aho)
795 are built by considering beads at the position of α -carbons in the crystal structures and introducing a
796 network of stiff harmonic bonds that maintains the secondary and tertiary structure of the NTRs. This
797 network of bonds is represented by the harmonic potential $\phi_{\text{network}} = K(r - b)^2$, where K is 8000
798 kJ/nm² and b is the original distance between the amino acid beads in the crystal structure. A bond is
799 made between the beads if b is less than 1.4 nm. The missing regions in the crystal structures of Kap120
800 and Kap114 have around 75% of their residues in a coil conformation calculated using PSIPRED⁹⁶, and
801 are included in the coarse-grained model as disordered regions.

802

803 For polyPR-polyPR interaction, we take into account hydrophobic/hydrophilic and electrostatic
804 interactions. The hydrophobic/hydrophilic interactions are represented by:

805

$$\phi_{\text{hp}} = \begin{cases} \varepsilon_{\text{rep}} \left(\frac{\sigma}{r} \right)^8 - \varepsilon_{ij} \left[\frac{4}{3} \left(\frac{\sigma}{r} \right)^6 - \frac{1}{3} \right] & r \leq \sigma \\ (\varepsilon_{\text{rep}} - \varepsilon_{ij}) \left(\frac{\sigma}{r} \right)^8 & r \geq \sigma, \end{cases}$$

806 where $\varepsilon_{ij} = \varepsilon_{\text{hp}} \sqrt{(\varepsilon_i \varepsilon_j)^{0.27}}$ is the strength of the interaction for each pair of amino acids (i,j) and $\sigma =$
807 0.6 nm. The values of ε_{hp} and ε_{rep} are 13 and 10 kJ/mol, respectively. The relative hydrophobic
808 strength values ($\varepsilon_i \in [0,1]$) of the different amino acids are listed in Table 3. The hydrophobic strength
809 values of charged residues are slightly increased compared to the original model⁹⁵ in line with our
810 recent work⁸⁶.

811

812 The electrostatic interactions between charged residues are described by the modified Coulomb law:

813

$$\phi_{\text{elec}} = \frac{q_i q_j}{4\pi \varepsilon_0 \varepsilon_r(r) r} e^{-\kappa r},$$

814 where $\varepsilon_r(r) = S_s \left[1 - \frac{r^2}{z^2} \frac{e^{r/z}}{(e^{r/z} - 1)^2} \right]$ is the distance-dependent dielectric constant of the solvent with
815 $S_s = 80$ and $z = 0.25$ nm. The value of the Debye screening coefficient, κ , is 1 nm^{-1} for monovalent
816 salt concentration $C_{\text{salt}} = 100 \text{ mM}$, and 1.5 nm^{-1} for $C_{\text{salt}} = 200 \text{ mM}$.

817

818 The interactions between polyPR and NTRs can be classified in three categories: electrostatic
819 interactions, cation-pi interactions, and excluded volume interactions. For electrostatic interactions,
820 we use the same electrostatic potential (ϕ_{elec}) as described above. To take into account the cation-pi
821 interactions between Arginine (in polyPR) and the aromatic residues F, Y, and W (in the NTRs), we use
822 an 8-6 Lennard-Jones (LJ) potential that replaces ϕ_{hp} for the RF, RY, and RW interactions:

823

$$\phi_{\text{cp,ij}}(r) = \varepsilon_{\text{cp,ij}} \left[3 \left(\frac{r_m}{r} \right)^8 - 4 \left(\frac{r_m}{r} \right)^6 \right].$$

824 The parameter r_m , which is the distance at which $\phi_{\text{cp,ij}}$ reaches its minimum value, is set to 0.45 nm
825 equal to the weighted average distance between the guanidinium group of Arginine and an aromatic
826 ring at different orientations (Planar, Oblique, Orthogonal)⁹⁷. To find $\varepsilon_{\text{cp,ij}}$ for the different cation-pi
827 pairs, we set the RY cation-pi energy as a basis for calculating the cation-pi energies for RF and RW
828 using PDB statistics. According to all-atom free energy calculations, the RY interaction energy is
829 comparable to the strongest interaction between different non-charged residues at physiological salt
830 concentrations⁹⁸. Therefore, in order for the cation-pi interactions to be compatible with the 1BPA
831 force field, we set $\varepsilon_{\text{cp,RY}} = 5 \text{ kJ/mol}$ which is similar to the deepest potential depth in the 1BPA force
832 field (5.2 kJ/mol). To estimate the energy difference between RY and the other combinations, similar
833 to⁹⁹, we use the PDB cation-pi contact frequencies in an aqueous environment¹⁰⁰, and a formulation

834 for statistical potential^{99,101}. In a dataset analyzed in¹⁰⁰, the frequencies of R, F, Y, and W are $p(R) =$
835 10919 , $p(F) = 9162$, $p(Y) = 8309$, $p(W) = 3412$, respectively, and the cation-pi contact
836 frequencies for RF, RY, and RW are $p(RF) = 630$, $p(RY) = 749$, $p(RW) = 609$. Based on these values
837 the energy differences between different cation-pi pairs can be estimated. As an example, using $k_B T \approx$
838 2.5 kJ/mol at $T = 300$ K, the energy difference between RY and RF (former minus latter) can be
839 estimated as $-k_B T \ln([p(RY)/p(RF)][p(F)/p(Y)]) \approx -0.7$ kJ/mol. The value of $\varepsilon_{cp,RF}$ is then
840 $\varepsilon_{cp,RF} \approx \varepsilon_{cp,RY} - 0.7$ kJ/mol ≈ 4.3 kJ/mol. A similar calculation results in $\varepsilon_{cp,RW} = 6.70$ kJ/mol.

841

842 For the hydrophilic/hydrophobic interactions between poly-PR and the rest of the NTR residues (the
843 orange residues in Fig 7A), we use ϕ_{hp} with $\varepsilon_{ij} = 10$ kJ/mol which leads to an excluded volume
844 potential that vanishes at $r = 0.6$ nm. For the interactions between the residues within the disordered
845 regions of NTRs, we use the 1BPA force field featuring ϕ_{hp} and ϕ_{elec} as described above.

846

Table 3. Relative hydrophobic strength values of the different amino acids

Amino acid	ε_i	Amino acid	ε_i
A	0.7	L	1
R	0.005	K	0.005
N	0.33	M	0.78
D	0.005	F	1
C	0.68	P	0.65
Q	0.64	S	0.45
E	0.005	T	0.51
G	0.41	W	0.96
H	0.53	Y	0.82
I	0.98	V	0.94

847

848 **Simulation and contact analysis**

849 Langevin dynamics simulations are performed at 300 K at monovalent salt concentrations of 100 mM
850 and 200 mM in NVT ensembles with a time-step of 0.02 ps and a Langevin friction coefficient of 0.02
851 ps⁻¹ using GROMACS version 2018. Simulations are performed for at least 2.5 μ s in cubic periodic boxes,
852 and the last 2 μ s are used for the contact analysis. The time-averaged number of contacts C_t between
853 the polyPR and NTRs is obtained by summing the number of contacts per time frame (i.e. the number
854 of polyPR/NTR residue pairs that are within 1 nm) over all frames and dividing by the total number of
855 frames. The error bars in Fig 7B are half of the standard deviation. The structures in Fig 7 are drawn
856 using VMD¹⁰².

857

858

859

860

861

862

863

864

865

866

867

868

869

870

Table 4 Yeast strains used in this study.

Strains are all in BY4741 genetic background:

Strains are in BY4741 genetic background		
BY4741 yeast	MATa <i>his3Δ1 leu2Δ0 met15Δ0 ura3Δ0</i>	Invitrogen
γMS01 pRS416-mCerulean-PR	BY4741 carrying pMS01	This study
γMS02 pRS416-mCerulean-GA	BY4741 carrying pMS02	This study
γMS03 GFP + pRS416	BY4741 <i>his3Δ1::GFP(pGal1)-HIS3</i> (pPP043) carrying pRS416	This study
γMS04 GFP + 416-PR	BY4741 <i>his3Δ1::GFP(pGal1)-HIS3</i> (pPP043) carrying pRS416-GAL-PR50	This study
γMS05 GFP + 416-GA	BY4741 <i>his3Δ1::GFP(pGal1)-HIS3</i> (pPP043) carrying pRS416-GAL-GA50	This study
γMS06 GFP-NLSSv40 + pRS416	BY4741 <i>his3Δ1::GFP-tcNLS(pGal1)-HIS3</i> (pPP042) carrying pRS416	This study
γMS07/08 GFP-NLSSv40 + 416-PR/GA	BY4741 <i>his3Δ1::GFP-tcNLS(pGal1)-HIS3</i> (pPP042) carrying pRS416-GAL-PR50 or pRS416-GAL-GA50	This study
γMS09-11 GFP-NES _{SSb1} + pRS416/PR/GA	BY4741 <i>his3Δ1::GFP-NESSb1(pGal1)-HIS3</i> (pPP046) carrying pRS416; pRS416-GAL-PR50 or pRS416-GAL-GA50	This study
γMS12-14 GFP-NLS _{Npm1} + pRS416/PR/GA	BY4741 <i>his3Δ1::GFP-Npm1NLS(pGal1)-HIS3</i> (pRAH23) carrying pRS416; pRS416-GAL-PR50 or pRS416-GAL-GA50	This study
γMS15-17 GFP-NLS _{Nab2} + pRS416/PR/GA	BY4741 <i>his3Δ1::GFP-Nab2NLS(pGal1)-HIS3</i> (pAA8) carrying pRS416; pRS416-GAL-PR50 or pRS416-GAL-GA50	This study
γMS18-20 GFP-NLS _{Pho4} + pRS416/PR/GA	BY4741 <i>his3Δ1::GFP-Pho4NLS(pGal1)-HIS3</i> (pAA9) carrying pRS416; pRS416-GAL-PR50 or pRS416-GAL-GA50	This study
γSMY16 AT1.03 ^{ymEGFPΔ11-ymScarletI}	ATP sensor	This study
	BY4741 <i>his3Δ1::pTEF1-his6-ymEGFPΔ11-B.subtilis ε-ymScarletI-HIS3</i> (pSM08)	
γMS21/22 ATP sensor + pRS416-PR/GA	BY4741 <i>his3Δ1::pTEF1-his6-ymEGFPΔ11-B.subtilis ε-ymScarletI-his3</i> (pSM08)	This study
BG1805-RanGEF OE	BY4741 <i>his3Δ1::GFP-SRM1(pGal1)-his3</i>	Dharmacon
BG1805-RanGAP OE	BY4741 <i>his3Δ1::GFP-RanGAP(pGal1)-his3</i>	Dharmacon
MS23-26 RanGEF OE + reporters	BY4741 <i>his3Δ1::GFP-RanGEF(pGal1)-his3</i> Carrying pPP042, pPP046, pAA8, or pAA9	This study
MS27-30 RanGAP OE + reporters	BY4741 <i>his3Δ1::GFP-RNA1(pGal1)-his3</i> Carrying pPP042, pPP046, pAA8, or pAA9	This study
Sxm1Δ	MATa <i>ura3Δ0 leu2Δ0 his3Δ1 met15Δ0 YDR395W::kanMX4</i>	Invitrogen
Kap114Δ	MATa <i>ura3Δ0 leu2Δ0 his3Δ1 met15Δ0 YGL241W::kanMX4</i>	Invitrogen
Kap120Δ	MATa <i>ura3Δ0 leu2Δ0 his3Δ1 met15Δ0 YPL125W::kanMX4</i>	Invitrogen
Kap122Δ	MATa <i>ura3Δ0 leu2Δ0 his3Δ1 met15Δ0 YGL016W::kanMX4</i>	Invitrogen
Kap123Δ	MATa <i>ura3Δ0 leu2Δ0 his3Δ1 met15Δ0 YER110C::kanMX4</i>	Invitrogen
MS31-34 Sxm1Δ + reporters	MATa <i>ura3Δ0 leu2Δ0 his3Δ1 met15Δ0 YDR395W::kanMX4</i> Carrying pPP042, pPP046, pAA8, or pAA9	This study
γMS35-38 Kap114Δ + reporters	MATa <i>ura3Δ0 leu2Δ0 his3Δ1 met15Δ0 YGL241W::kanMX4</i> Carrying pPP042, pPP046, pAA8, or pAA9	This study
γMS39-42 Kap120Δ + reporters	MATa <i>ura3Δ0 leu2Δ0 his3Δ1 met15Δ0 YPL125W::kanMX4</i> Carrying pPP042, pPP046, pAA8, or pAA9	This study
γMS43-46 Kap122Δ + reporters	MATa <i>ura3Δ0 leu2Δ0 his3Δ1 met15Δ0 YGL016W::kanMX4</i> Carrying pPP042, pPP046, pAA8, or pAA9	This study
γMS47-50 Kap123Δ + reporters	MATa <i>ura3Δ0 leu2Δ0 his3Δ1 met15Δ0 YER110C::kanMX4</i> Carrying pPP042, pPP046, pAA8, or pAA9	This study
γMS51-86 NTR-GFP + 416-PR/GA	BY4741 MATa <i>his3Δ1 leu2Δ0 met15Δ0 ura3Δ0::XX-GFP-his3MX6</i> where XX is: Crm1, CSe1, Srp1, Rsl1, Kap104, Kap114, Los1, Lph2, Mex67, Msn5, Mtr10, Nmd5, Pdr6, Pse1, Sxm1, Yrb4, Srm1, Rna1	Thermofisher

Plasmids:

pAG416-GAL-PR ₅₀	Jovicic et al. ³⁵ ; Addgene plasmid #84901; http://n2t.net/addgene:84901
pAG416-GAL-GA ₅₀	Jovicic et al. ³⁵ ; Addgene plasmid #84903; http://www.addgene.org/84903/
pAG303-GAL-PR ₅₀	Jovicic et al. ³⁵ ; Addgene plasmid #84905; http://www.addgene.org/84905/
pAG303-GAL-PA ₅₀	Jovicic et al. ³⁵ ; Addgene plasmid #84906; http://www.addgene.org/84906/
pAG303-GAL-GA ₅₀	Jovicic et al. ³⁵ ; Addgene plasmid #84907; http://www.addgene.org/84907/
pAG303-GAL-GR ₁₀₀	Jovicic et al. ³⁵ ; Addgene plasmid #84908; http://www.addgene.org/84908/
pMS01 pRS416-mCerulean-PR ₅₀	This study
pMS02 pRS416-mCerulean-GA ₅₀	This study
pPP042 pRS303-GFP-tcNLS(<i>pGal1</i>)	Rempel et al. ⁷²

934	pPP043 pRS303-GFP	Rempel et al. ⁷²
935	pPP046 pRS303-GFP-NES _{Ssb1}	Rempel et al. ⁷²
936	pAA8 pRS303-NLS _{Nab2} -GFP	Timney et al. ⁶⁶
937	pAA9 pRS303-NLS _{Pho4} -GFP	Timney et al. ⁶⁶
938	pRAH23 pRS303-NPM1-GFP	Lokareddy et al. ¹⁰³
939	pSM08 pRS303-pTEF1-his6-ymEGFPΔ11-B.subtilis ε-ymScarletI	This study
940		

941 **Acknowledgments:** This work was financially supported by the Netherlands Organization for Scientific
942 Research (NWO BBOL 737.016.016 to LMV and P.R.O) and NWO-Vici (VI.C.192.031) to LMV. We thank
943 Thamar Jessurun Lobo and Prof. Victor Guryev for their help with the PCA and cluster analysis. We
944 thank Prof. Michael Chang and all members from the Veenhoff and Chang laboratories for their critical
945 input in the project.

946 **Competing interests:** The authors declare that no competing interests exists.

947 **Source data files:**

948 1. SRM proteomics data, figure 2
949 2. Untargeted proteomics data, cargo abundances
950 3. Raw N/C ratios, figure 3
951 4. Raw N/C ratios, figure 4
952 5. Raw N/C ratios, figure 5
953 6. NTR charge, figure 7
954

955 **References**

956 1. Fernandez-Martinez, J. & Rout, M. P. One Ring to Rule them All? Structural and Functional Diversity in the Nuclear Pore Complex.
957 *Trends Biochem. Sci.* **46**, 595–607 (2021).

958 2. Lowe, A. R. et al. Importin-β modulates the permeability of the nuclear pore complex in a Ran-dependent manner. *Elife* **4**, e04052
959 (2015).

960 3. Wozniak, R. W., Rout, M. P. & Aitchison, J. D. Karyopherins and kissing cousins. *Trends in Cell Biology* vol. 8 184–188 (1998).

961 4. Titov, A. A. & Blobel, G. The karyopherin Kap122p/Pdr6p imports both subunits of the transcription factor IIA into the nucleus. *J. Cell Biol.* **147**, 235–245 (1999).

962 5. Allen, N. P. C. et al. Deciphering networks of protein interactions at the nuclear pore complex. *Mol. Cell. Proteomics* **1**, 930–946
963 (2002).

964 6. Kose, S., Furuta, M. & Imamoto, N. Hikeshi, a nuclear import carrier for Hsp70s, protects cells from heat shock-induced nuclear
965 damage. *Cell* **149**, 578–589 (2012).

966 7. Kosyna, F. & Depping, R. Controlling the Gatekeeper: Therapeutic Targeting of Nuclear Transport. *Cells* **7**, 221 (2018).

967 8. Pumroy, R. A. & Cingolani, G. Diversification of importin-α isoforms in cellular trafficking and. *Biochemical Journal* vol. 466 13–28
968 (2015).

969 9. Baade, I. & Kehlenbach, R. H. The cargo spectrum of nuclear transport receptors. *Current Opinion in Cell Biology* vol. 58 1–7
970 (2019).

971 10. Bischoff, F. R. & Görlich, D. RanBP1 is crucial for the release of RanGTP from importin β-related nuclear transport factors. *FEBS Lett.* **419**, 249–254 (1997).

972 11. Cautain, B., Hill, R., de Pedro, N. & Link, W. Components and regulation of nuclear transport processes. *FEBS J.* **282**, 445–462
973 (2015).

974 12. Lolodi, O., Yamazaki, H., Otsuka, S., Kumeta, M. & Yoshimura, S. H. Dissecting in vivo steady-state dynamics of Karyopherin-
975 dependent nuclear transport. *Mol. Biol. Cell* **27**, 167–176 (2016).

976 13. Ogawa, Y. & Imamoto, N. Nuclear transport adapts to varying heat stress in a multistep mechanism. *J. Cell Biol.* **217**, 2341 (2018).

977 14. Furuta, M. et al. Heat-shock induced nuclear retention and recycling inhibition of importin α. *Genes to Cells* **9**, 429–441 (2004).

978 15. Miyamoto, Y. et al. Cellular stresses induce the nuclear accumulation of importin α and cause a conventional nuclear import
979 block. *J. Cell Biol.* **165**, 617–623 (2004).

980 16. Saavedra, C., Tuug, K. S., Amberg, D. C., Hopper, A. K. & Cole, C. N. Regulation of mRNA export in response to stress in

983 *Saccharomyces cerevisiae. Genes Dev.* **10**, 1608–1620 (1996).

984 17. Huang, H. Y. & Hopper, A. K. Separate responses of karyopherins to glucose and amino acid availability regulate
985 nucleocytoplasmic transport. *Mol. Biol. Cell* **25**, 2840 (2014).

986 18. Stochaj, U., Rassadi, R. & Chiu, J. Stress-mediated inhibition of the classical nuclear protein import pathway and nuclear
987 accumulation of the small GTPase Gsp1p. *FASEB J.* **14**, 2130–2132 (2000).

988 19. Chughtai, Z. S., Rassadi, R., Matusiewicz, N. & Stochaj, U. Starvation Promotes Nuclear Accumulation of the hsp70 Ssa4p in Yeast
989 Cells *. *J. Biol. Chem.* **276**, 20261–20266 (2001).

990 20. DeVit, M. J. & Johnston, M. The nuclear exportin Msn5 is required for nuclear export of the Mig1 glucose repressor of
991 *Saccharomyces cerevisiae. Curr. Biol.* **9**, 1231–1241 (1999).

992 21. Kelley, J. B. & Paschal, B. M. Hyperosmotic stress signaling to the nucleus disrupts the ran gradient and the production of RanGTP.
993 *Mol. Biol. Cell* **18**, 4365–4376 (2007).

994 22. Ferrigno, P., Posas, F., Koepp, D., Saito, H. & Silver, P. A. Regulated nucleo/cytoplasmic exchange of HOG1 MAPK requires the
995 importin beta homologs NMD5 and XPO1. *EMBO J.* **17**, 5606 (1998).

996 23. Kodiha, M. *et al.* Oxidative stress mislocalizes and retains transport factor importin-alpha and nucleoporins Nup153 and Nup88 in
997 nuclei where they generate high molecular mass complexes. *Biochim. Biophys. Acta* **1783**, 405–418 (2008).

998 24. Kodiha, M., Chu, A., Matusiewicz, N. & Stochaj, U. Multiple mechanisms promote the inhibition of classical nuclear import upon
999 exposure to severe oxidative stress. *Cell Death Differ.* **11**, 862–874 (2004).

1000 25. Yasuda, Y., Miyamoto, Y., Saiwaki, T. & Yoneda, Y. Mechanism of the stress-induced collapse of the Ran distribution. *Exp. Cell Res.*
1001 **312**, 512–520 (2006).

1002 26. Crampton, N., Kodiha, M., Shrivastava, S., Umar, R. & Stochaj, U. Oxidative Stress Inhibits Nuclear Protein Export by Multiple
1003 Mechanisms That Target FG Nucleoporins and Crm1. *Mol. Biol. Cell* **20**, 5106 (2009).

1004 27. Grima, J. C. *et al.* Mutant Huntingtin Disrupts the Nuclear Pore Complex. *Neuron* **94**, 93 (2017).

1005 28. Eftekharzadeh, B. *et al.* Tau Protein Disrupts Nucleocytoplasmic Transport in Alzheimer’s Disease. *Neuron* **99**, 925–940.e7 (2018).

1006 29. Chou, C.-C. *et al.* TDP-43 pathology disrupts nuclear pore complexes and nucleocytoplasmic transport in ALS/FTD. *Nat. Neurosci.*
1007 **21**, 228–239 (2018).

1008 30. Dormann, D. *et al.* ALS-associated fused in sarcoma (FUS) mutations disrupt transportin-mediated nuclear import. *EMBO J.* **29**,
1009 2841–2857 (2010).

1010 31. Woerner, A. C. *et al.* Cytoplasmic protein aggregates interfere with nucleocytoplasmic transport of protein and RNA. *Science* **351**,
1011 173–6 (2016).

1012 32. Green, K. M., Linsalata, A. E. & Todd, P. K. RAN translation—What makes it run? *Brain Res.* **1647**, 30–42 (2016).

1013 33. Ash, P. E. A. *et al.* Unconventional translation of C9ORF72 GGGGCC expansion generates insoluble polypeptides specific to
1014 c9FTD/ALS. *Neuron* **77**, 639–46 (2013).

1015 34. Mori, K. *et al.* The C9orf72 GGGGCC repeat is translated into aggregating dipeptide-repeat proteins in FTLD/ALS. *Science* **339**,
1016 1335–8 (2013).

1017 35. Jovičić, A. *et al.* Modifiers of C9orf72 dipeptide repeat toxicity connect nucleocytoplasmic transport defects to FTD/ALS. *Nat.*
1018 *Neurosci.* **18**, 1226–9 (2015).

1019 36. Wen, X. *et al.* Antisense proline-arginine RAN dipeptides linked to C9ORF72-ALS/FTD form toxic nuclear aggregates that initiate
1020 invitro and invivo neuronal death. *Neuron* **84**, 1213–1225 (2014).

1021 37. Lee, K.-H. K. H. H. *et al.* C9orf72 Dipeptide Repeats Impair the Assembly, Dynamics, and Function of Membrane-Less Organelles.
1022 *Cell* **167**, 774–788.e17 (2016).

1023 38. Rudich, P. *et al.* Nuclear localized C9orf72-associated arginine-containing dipeptides exhibit age-dependent toxicity in *C. elegans*.
1024 *Hum. Mol. Genet.* **26**, 4916–4928 (2017).

1025 39. Tao, Z. *et al.* Nucleolar stress and impaired stress granule formation contribute to C9orf72 RAN translation-induced cytotoxicity.
1026 *Hum. Mol. Genet.* **24**, 2426–2441 (2015).

1027 40. Semmelink, M. F. W., Steen, A. & Veenhoff, L. M. Measuring and Interpreting Nuclear Transport in Neurodegenerative Disease—
1028 The Example of C9orf72 ALS. *Int. J. Mol. Sci.* **22**, (2021).

1029 41. Haeusler, A. R., Donnelly, C. J. & Rothstein, J. D. The expanding biology of the C9orf72 nucleotide repeat expansion in
1030 neurodegenerative disease. *Nat Rev Neurosci* **17**, 383–395 (2016).

1031 42. Taylor, J. P., Brown, R. H. & Cleveland, D. W. Decoding ALS: from genes to mechanism. *Nature* **539**, 197–206 (2016).

1032 43. Huttun, S. & Dormann, D. Nucleocytoplasmic transport defects in neurodegeneration — Cause or consequence? *Seminars in Cell*
1033 *and Developmental Biology* (2019) doi:10.1016/j.semcd.2019.05.020.

1034 44. Vanneste, J. & Van Den Bosch, L. The Role of Nucleocytoplasmic Transport Defects in Amyotrophic Lateral Sclerosis. *Int J Mol Sci.*
1035 **22**, 12175 (2021).

1036 45. Chandra, S. & Lusk, C. P. Emerging Connections between Nuclear Pore Complex Homeostasis and ALS. *Int. J. Mol. Sci.* **23**, (2022).

1037 46. Xiao, S. *et al.* Isoform-specific antibodies reveal distinct subcellular localizations of C9orf72 in amyotrophic lateral sclerosis. *Ann.*
1038 *Neurol.* **78**, 568–583 (2015).

1039 47. Zhang, K. *et al.* The C9orf72 repeat expansion disrupts nucleocytoplasmic transport. *Nature* **525**, 56–61 (2015).

1040 48. Zhang, Y.-J. *et al.* C9ORF72 poly(GA) aggregates sequester and impair HR23 and nucleocytoplasmic transport proteins. *Nat.*
1041 *Neurosci.* **19**, 668–77 (2016).

1042 49. Frottin, F., Pérez-Berlanga, M., Hartl, F. U. & Hipp, M. S. Multiple pathways of toxicity induced by C9orf72 dipeptide repeat
1043 aggregates and G4C2 RNA in a cellular model. *Elife* **10**, (2021).

1044 50. Freibaum, B. D. *et al.* GGGGCC repeat expansion in C9orf72 compromises nucleocytoplasmic transport. *Nature* **525**, 129–133
1045 (2015).

1046 51. Hayes, L. R., Duan, L., Bowen, K., Kalab, P. & Rothstein, J. D. C9orf72 arginine-rich dipeptide repeat proteins disrupt karyopherin-
1047 mediated nuclear import. *Elife* **9**, (2020).

1048 52. Shi, K. Y. *et al.* Toxic PRn poly-dipeptides encoded by the C9orf72 repeat expansion block nuclear import and export. *Proc. Natl.*
1049 *Acad. Sci. U. S. A.* 201620293 (2017) doi:10.1073/pnas.1620293114.

1050 53. Kinoshita, Y. *et al.* Nuclear Contour Irregularity and Abnormal Transporter Protein Distribution in Anterior Horn Cells in
1051 Amyotrophic Lateral Sclerosis. *J. Neuropathol. Exp. Neurol.* **68**, (2009).

1052 54. Coyne, A. N. *et al.* Nuclear accumulation of CHMP7 initiates nuclear pore complex injury and subsequent TDP-43 dysfunction in
1053 sporadic and familial ALS. *Sci. Transl. Med* **13**, 1923 (2021).

1054 55. Huttun, S. *et al.* Nuclear Import Receptors Directly Bind to Arginine-Rich Dipeptide Repeat Proteins and Suppress Their
1055 Pathological Interactions. *Cell Rep.* **33**, 108538 (2020).

1056 56. Khosravi, B. *et al.* Cytoplasmic poly-GA aggregates impair nuclear import of TDP-43 in C9orf72 ALS/FTLD. *Hum. Mol. Genet.* **26**,
1057 790–800 (2017).

1058 57. Vanneste, J. *et al.* C9orf72-generated poly-GR and poly-PR do not directly interfere with nucleocytoplasmic transport. *Sci. Rep.* **9**,
1059 (2019).

1060 58. Ramic, M. *et al.* Epigenetic Small Molecules Rescue Nucleocytoplasmic Transport and DNA Damage Phenotypes in C9ORF72
1061 ALS/FTD. *Brain Sci.* **11**, (2021).

1062 59. Zhang, Y.-J. *et al.* Aggregation-prone c9FTD/ALS poly(GA) RAN-translated proteins cause neurotoxicity by inducing ER stress. *Acta*
1063 *Neuropathol.* **128**, 505–24 (2014).

1064 60. Kwon, I. *et al.* Poly-dipeptides encoded by the C9orf72 repeats bind nucleoli, impede RNA biogenesis, and kill cells. *Science* **345**,
1065 1139–45 (2014).

1066 61. Chew, J. *et al.* Neurodegeneration. C9ORF72 repeat expansions in mice cause TDP-43 pathology, neuronal loss, and behavioral
1067 deficits. *Science* **348**, 1151–4 (2015).

1068 62. Crane, M. M., Clark, I. B. N., Bakker, E., Smith, S. & Swain, P. S. A microfluidic system for studying ageing and dynamic single-cell
1069 responses in budding yeast. *PLoS One* **9**, (2014).

1070 63. Yang, D. *et al.* FTD/ALS-associated poly(GR) protein impairs the Notch pathway and is recruited by poly(GA) into cytoplasmic
1071 inclusions. *Acta Neuropathol.* **130**, 525–35 (2015).

1072 64. Lopez-Gonzalez, R. *et al.* Poly(GR) in C9ORF72-Related ALS/FTD Compromises Mitochondrial Function and Increases Oxidative
1073 Stress and DNA Damage in iPSC-Derived Motor Neurons. *Neuron* **92**, 383–391 (2016).

1074 65. Callister, J. B., Ryan, S., Sim, J., Rollinson, S. & Pickering-Brown, S. M. Modelling C9orf72 dipeptide repeat proteins of a
1075 physiologically relevant size. *Hum. Mol. Genet.* ddw327 (2016) doi:10.1093/hmg/ddw327.

1076 66. Timney, B. L. *et al.* Simple kinetic relationships and nonspecific competition govern nuclear import rates in vivo. *J. Cell Biol.* **175**,
1077 579–593 (2006).

1078 67. Hodel, A. E. *et al.* Nuclear localization signal receptor affinity correlates with in vivo localization in *Saccharomyces cerevisiae*. *J.*
1079 *Biol. Chem.* **281**, 23545–23556 (2006).

1080 68. Kopito, R. B. & Elbaum, M. Nucleocytoplasmic transport: A thermodynamic mechanism. *HFSP J.* **3**, 130–141 (2009).

1081 69. Boeynaems, S. *et al.* Drosophila screen connects nuclear transport genes to DPR pathology in c9ALS/FTD. *Sci. Rep.* **6**, 20877

1082 (2016).

1083 70. Imamura, H. *et al.* Visualization of ATP levels inside single living cells with fluorescence resonance energy transfer-based
1084 genetically encoded indicators. *Proc. Natl. Acad. Sci. U. S. A.* **106**, 15651–15656 (2009).

1085 71. Schwobebel, E. D., Ho, T. H. & Moore, M. S. The mechanism of inhibition of Ran-dependent nuclear transport by cellular ATP
1086 depletion. *J. Cell Biol.* **157**, 963–974 (2002).

1087 72. Rempel, I. L. *et al.* Age-dependent deterioration of nuclear pore assembly in mitotic cells decreases transport dynamics. *Elife* **8**,
1088 (2019).

1089 73. Popken, P., Ghavami, A., Onck, P. R., Poolman, B. & Veenhoff, L. M. Size-dependent leak of soluble and membrane proteins
1090 through the yeast nuclear pore complex. *Mol. Biol. Cell* **26**, 1386–94 (2015).

1091 74. Timney, B. L. *et al.* Simple rules for passive diffusion through the nuclear pore complex. *J. Cell Biol.* (2016).

1092 75. Shulga, N., James, P., Craig, E. A. & Goldfarb, D. S. A nuclear export signal prevents *Saccharomyces cerevisiae* Hsp70 Ssb1p from
1093 stimulating nuclear localization signal-directed nuclear transport. *J. Biol. Chem.* **274**, 16501–16507 (1999).

1094 76. Kalderon, D., Roberts, B. L., Richardson, W. D. & Smith, A. E. A short amino acid sequence able to specify nuclear location. *Cell* **39**,
1095 499–509 (1984).

1096 77. Robbins, J., Dilworth, S. M., Laskey, R. A. & Dingwall, C. Two interdependent basic domains in nucleoplasmin nuclear targeting
1097 sequence: Identification of a class of bipartite nuclear targeting sequence. *Cell* **64**, 615–623 (1991).

1098 78. Lee, D. C. Y. & Aitchison, J. D. Kap104p-mediated nuclear import. Nuclear localization signals in mRNA- binding proteins and the
1099 role of Ran and RNA. *J. Biol. Chem.* **274**, 29031–29037 (1999).

1100 79. Kaffman, A., Rank, N. M. & O’Shea, E. K. Phosphorylation regulates association of the transcription factor Pho4 with its import
1101 receptor Pse1/Kap121. *Genes Dev.* **12**, 2673–2683 (1998).

1102 80. Frey, S. *et al.* Surface Properties Determining Passage Rates of Proteins through Nuclear Pores. *Cell* **174**, 202–217.e9 (2018).

1103 81. Meinema, A. C., Poolman, B. & Veenhoff, L. M. Quantitative Analysis of Membrane Protein Transport Across the Nuclear Pore
1104 Complex. *Traffic* **14**, 487–501 (2013).

1105 82. Mouton, S. N. *et al.* A physicochemical perspective of aging from single-cell analysis of ph, macromolecular and organellar
1106 crowding in yeast. *Elife* **9**, 1–42 (2020).

1107 83. Hahn, J.-S., Hu, Z., Thiele, D. J. & Iyer, V. R. Genome-Wide Analysis of the Biology of Stress Responses through Heat Shock
1108 Transcription Factor. *Mol. Cell. Biol.* **24**, 5249 (2004).

1109 84. Mühlhofer, M. *et al.* The Heat Shock Response in Yeast Maintains Protein Homeostasis by Chaperoning and Replenishing
1110 Proteins. *Cell Rep.* **29**, 4593–4607.e8 (2019).

1111 85. Sévin, D. C., Stählin, J. N., Pollak, G. R., Kuehne, A. & Sauer, U. Global Metabolic Responses to Salt Stress in Fifteen Species. *PLoS
1112 One* **11**, e0148888 (2016).

1113 86. Jafarinia, H., van der Giessen, E. & Onck, P. R. Phase Separation of Toxic Dipeptide Repeat Proteins Related to C9orf72 ALS/FTD.
1114 *Biophys. J.* **119**, 843–851 (2020).

1115 87. Zhang, K. *et al.* Stress Granule Assembly Disrupts Nucleocytoplasmic Transport. *Cell* **173**, 958–971.e17 (2018).

1116 88. Friedman, A. K., Boeynaems, S. & Baker, L. A. Synthetic hydrogel mimics of the nuclear pore complex for the study of
1117 nucleocytoplasmic transport defects in C9orf72 ALS/FTD. *Anal. Bioanal. Chem.* **414**, 525–532 (2022).

1118 89. Boersma, A. J., Zuhorn, I. S. & Poolman, B. A sensor for quantification of macromolecular crowding in living cells. *Nat. Methods*
1119 **12**, 227–9, 1 p following 229 (2015).

1120 90. Shulga, N. *et al.* In vivo nuclear transport kinetics in *Saccharomyces cerevisiae*: a role for heat shock protein 70 during targeting
1121 and translocation. *J. Cell Biol.* **135**, 329–39 (1996).

1122 91. Schindelin, J. *et al.* Fiji: An open-source platform for biological-image analysis. *Nature Methods* vol. 9 676–682 (2012).

1123 92. Cohen, A. *et al.* Water-transfer slows aging in *Saccharomyces cerevisiae*. *PLoS One* **11**, (2016).

1124 93. Cox, J. & Mann, M. MaxQuant enables high peptide identification rates, individualized p.p.b.-range mass accuracies and
1125 proteome-wide protein quantification. *Nat. Biotechnol.* **26**, 1367–1372 (2008).

1126 94. Cox, J. *et al.* Accurate proteome-wide label-free quantification by delayed normalization and maximal peptide ratio extraction,
1127 termed MaxLFQ. *Mol. Cell. Proteomics* **13**, 2513–2526 (2014).

1128 95. Ghavami, A., Veenhoff, L. M., Van Der Giessen, E. & Onck, P. R. Probing the Disordered Domain of the Nuclear Pore Complex
1129 through Coarse-Grained Molecular Dynamics Simulations. *Biophys. J.* **107**, 1393 (2014).

1130 96. McGuffin, L. J., Bryson, K. & Jones, D. T. The PSIPRED protein structure prediction server. *Bioinformatics* **16**, 404–405 (2000).

1131 97. Crowley, P. B. & Golovin, A. Cation-pi interactions in protein-protein interfaces. *Proteins* **59**, 231–239 (2005).

1132 98. Krainer, G. *et al.* Reentrant liquid condensate phase of proteins is stabilized by hydrophobic and non-ionic interactions. *Nat. Commun.* **12**, (2021).

1134 99. Song, J., Ng, S. C., Tompa, P., Lee, K. A. W. & Chan, H. S. Polycation- π interactions are a driving force for molecular recognition by
1135 an intrinsically disordered oncoprotein family. *PLoS Comput. Biol.* **9**, (2013).

1136 100. Gallivan, J. P. & Dougherty, D. A. Cation-pi interactions in structural biology. *Proc. Natl. Acad. Sci. U. S. A.* **96**, 9459–9464 (1999).

1137 101. Miyazawa, S. & Jernigan, R. L. Estimation of effective interresidue contact energies from protein crystal structures: quasi-
1138 chemical approximation. *Macromolecules* **18**, 534–552 (1985).

1139 102. Humphrey, W., Dalke, A. & Schulten, K. VMD: visual molecular dynamics. *J. Mol. Graph.* **14**, 33–38 (1996).

1140 103. Lokareddy, R. K. *et al.* Distinctive Properties of the Nuclear Localization Signals of Inner Nuclear Membrane Proteins Heh1 and
1141 Heh2. *Structure* **23**, 1305–1316 (2015).

1142 104. Fanara, P., Hodel, M. R., Corbett, A. H. & Hodel, A. E. Quantitative Analysis of Nuclear Localization Signal (NLS)-Importin
1143 Interaction through Fluorescence Depolarization EVIDENCE FOR AUTO-INHIBITORY REGULATION OF NLS BINDING*. *J. Biol. Chem.*
1144 **275**, 21218–21223 (2000).

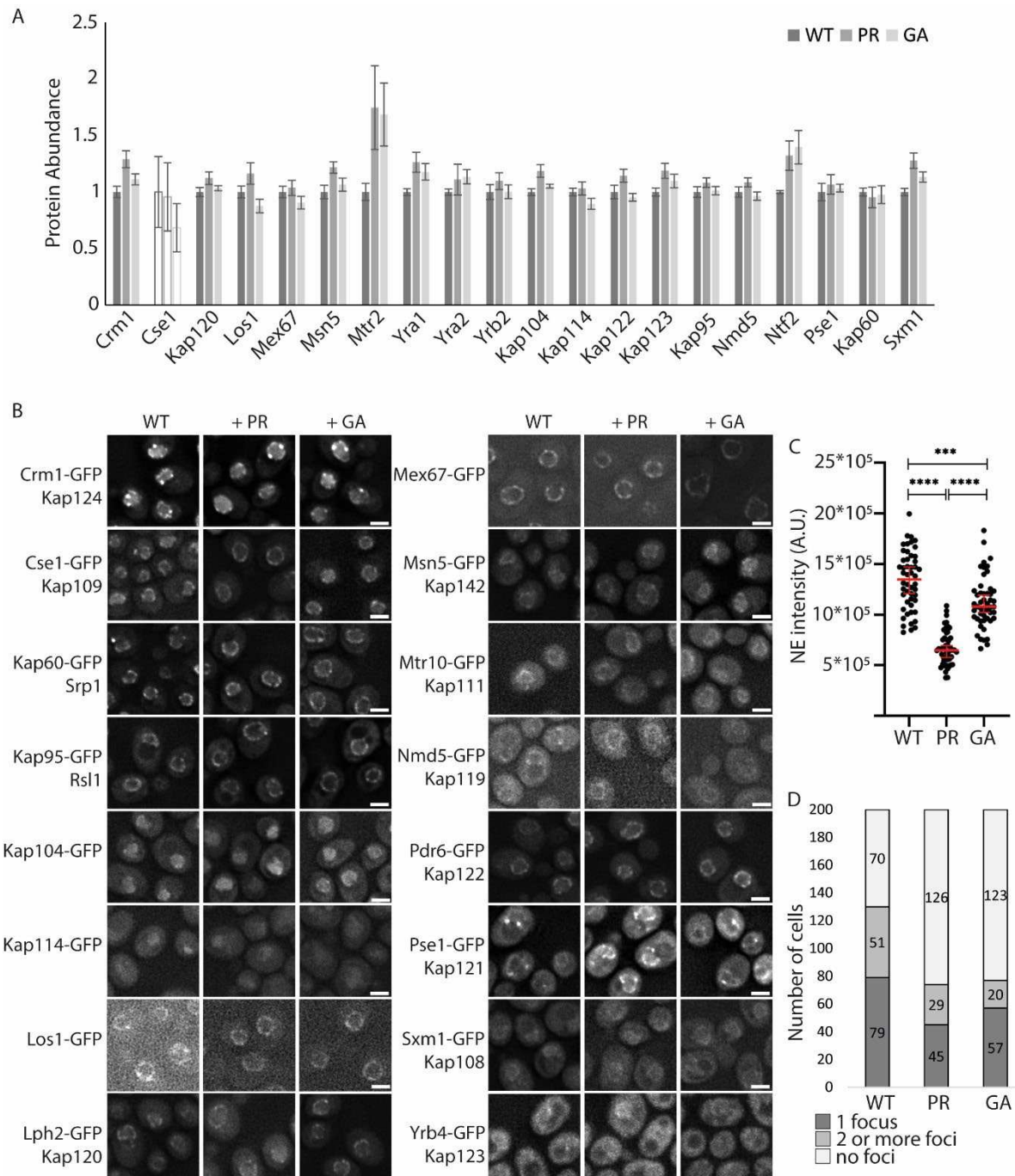
1145 105. Catimel, B. *et al.* Biophysical Characterization of Interactions Involving Importin- α during Nuclear Import *. *J. Biol. Chem.* **276**,
1146 34189–34198 (2001).

1147

1148

1149

1150 Supplementary



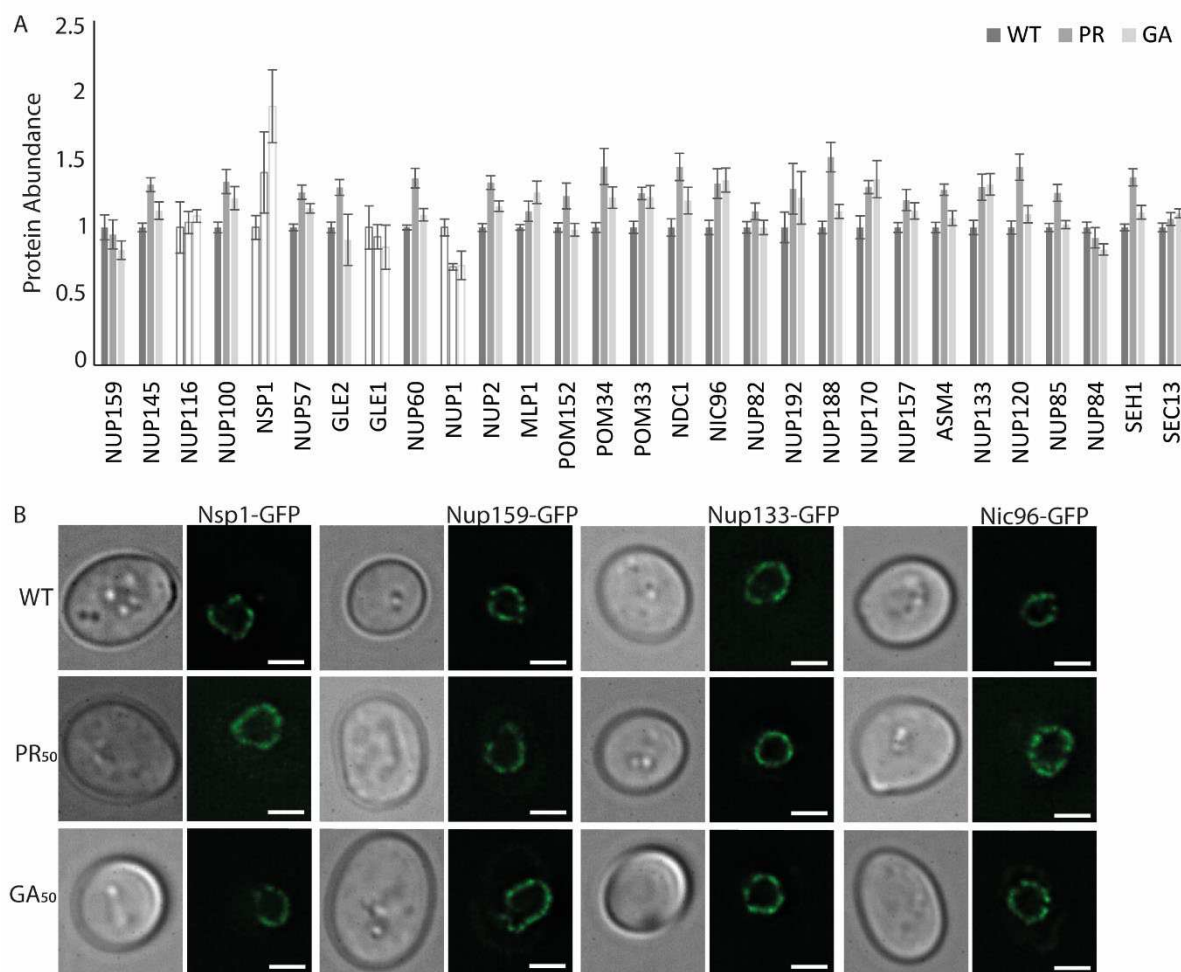
1151
1152 **Fig 2 – figure supplement 1. Abundance and localization of NTRs in polyPR and polyGA expressing cells.** **A)** Abundance of
1153 NTRs in whole cell extracts of WT or PR₅₀/GA₅₀-expressing cells determined by SRM-based proteomics in two biological and
1154 one technical replicate, except for Cse1 which has one replicate (in white bars). **B)** Localization of GFP-tagged NTRs expressed
1155 from native promotor and genomic location compared between WT cells and cells expressing PR₅₀ or GA₅₀; scale bar equals
1156 2μm. **C)** The intensity of Cse1-GFP at the nuclear envelope in WT, PR-expressing, and GA-expressing cells (all 50 cells). **D)** The
1157 number of Pse1-GFP foci in WT cells, or those expressing PR/GA.

1158

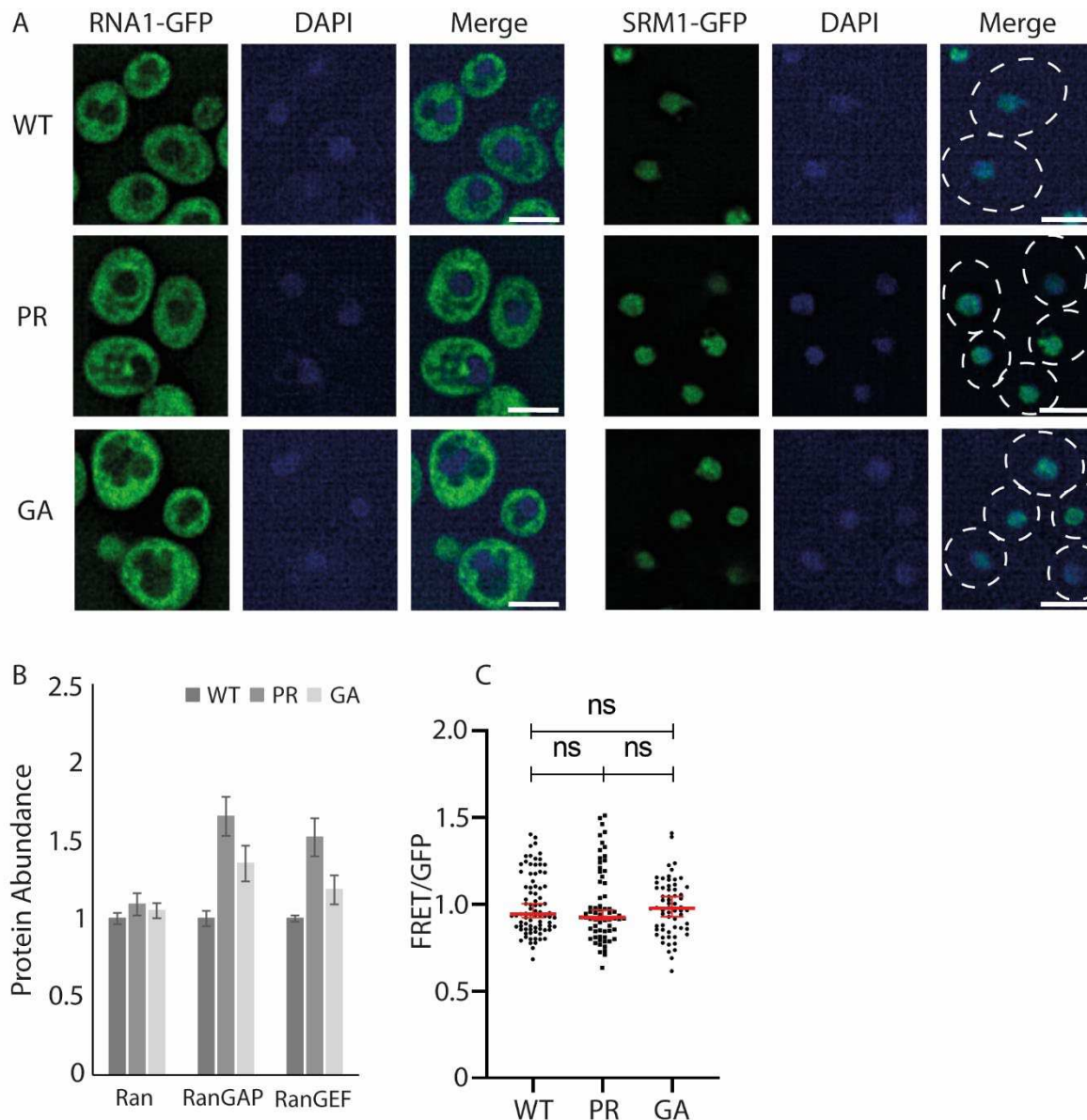
1159

1160

1161



1162
1163 **Fig 2 – figure supplement 2. Abundance and localization of nucleoporins in polyPR and polyGA expressing cells. A)**
1164 Abundance of nucleoporins in whole cell extracts of WT or PR₅₀/GA₅₀-expressing cells determined by SRM-based proteomics
1165 in two biological and one technical replicate, except for Nup116, Nsp1, Gle, Nup1 which have one replicate (in white bars).
1166 **B)** The localization of GFP-tagged Nsp1, Nup133, Nup159, and Nic96 does not change upon PR₅₀ expression; Nic96 and
1167 Nup133 also shown in Fig2. Scale bar equals 2μm.



1168
1169 **Fig 2 – figure supplement 3. Abundance and localization of Ran, RanGAP and RanGEF in polyPR and polyGA expressing**
1170 **cells. A)** The localization of GFP-tagged RanGAP and RanGEF does not change with PR₅₀ expression. RanGAP is cytoplasmic
1171 diffuse and RanGEF nuclear diffuse. Nuclear staining with DAPI, scale bar equals 2μm. Also shown in Fig 2. **B)** Abundance of
1172 Ran, RanGAP and RanGEF in whole cell extracts of WT or PR₅₀/GA₅₀-expressing cells determined by SRM-based proteomics in
1173 two biological and one technical replicate. **C)** A FRET-based ATP-sensor measures free ATP levels. The FRET over GFP ratio
1174 measured in live cells is not significantly changed between WT (n = 83) and PR-expressing cells (n = 67) or GA-expressing cells
1175 (n=62) as determined via the Mann-Whitney test.

1176

1177

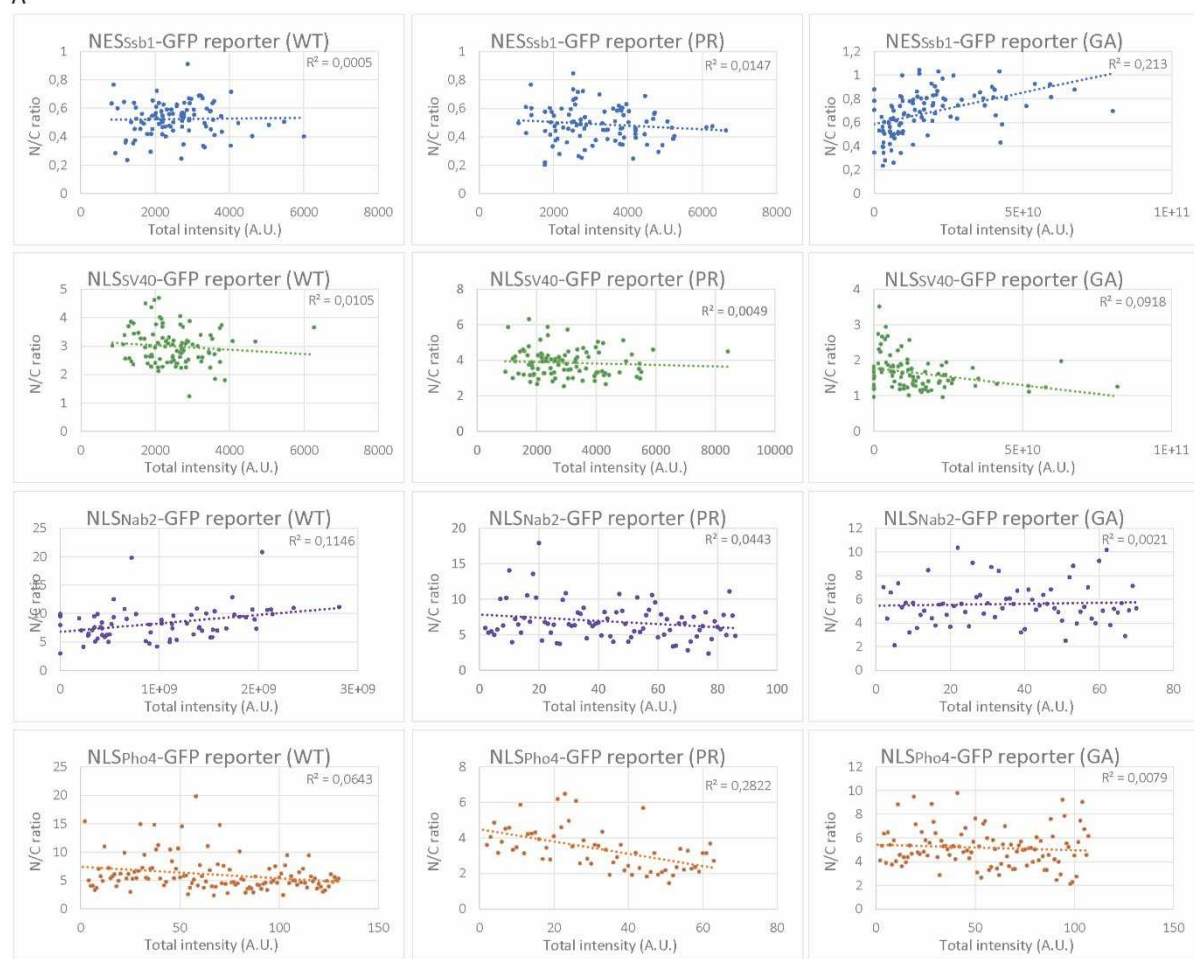
1178

1179

1180

1181

A



1182
1183
1184

Fig S1. Nuclear accumulation of transport reporters is independent of their expression level. A) N/C ratios from WT, PR₅₀- and GA₅₀-expressing cells show no correlation between expression level (total intensity of both N and C) and N/C ratios.

1185
1186
1187
1188
1189
1190
1191
1192
1193
1194
1195
1196
1197

Table S1 Characteristics of NTRs studied

NLS	Ssb1 NES	Sv40 NLS	Npm1 NLS	Nab2 NLS	Pho4 NLS
Karyopherin	Crm1	Kap60/95	Kap60/95	Kap104	PSE1
Human NTR homologue	Exportin	60: Karyopherin α 95: Karyopherin β	60: Karyopherin α 95: Karyopherin β	TNPO1	IPO5
Localization NTR (see Fig 2 – figure supplement 1B)	Nuclear + foci at nuclear ring	Nuclear ring	Nuclear ring	Nuclear	Foci at nuclear ring
Abundance NTR (molecules/cell) (according to SGD yeastgenome.org)	8276 \pm 2396	60: 8820 \pm 4085 95: 15792 \pm 5198	60: 8820 \pm 4085 95: 15792 \pm 5198	4755 \pm 2218	8125 \pm 1774
Used localization signal sequence	IEAALSDALA ALQI ⁷⁵	PKKKRKVDPKK KRKV ⁷⁶	AVKRPAATKK AGQKKKKLD ⁷⁷	DNSQRFTQRG GGAVGKNRRG GRGGGNRGGRN NNSTRFNPLAK ALGMAGESN ⁷⁸	ANKVTKNKS SSPYLNKRRGK PGPDSATSLFE LPDSVIPTPKP KPKPKNTPKVILP ⁷⁹
Binding affinity to NLS	X	60: 10nM ¹⁰⁴ Complex: 35nM ¹⁰⁵ Imp α to Imp β : 11-14nM ¹⁰⁵	60: 46 \pm 14nM ¹⁰³ Complex: 48nM ¹⁰⁵	17nM ⁶⁶	93nM ⁶⁶
Important cargo (according to SGD yeastgenome.org)	Proteins, RNAs, and ribosomal subunits	Nuclear proteins, ribosome-bound peptides	Nuclear proteins, ribosome-bound peptides	Nab2, Hrp1, RNA export splicing machinery	Pdr1p, Yap1p, Ste12p, and Aft1p

1198

Table S2 Steady state localization of transport reporters for nuclear transport by Crm1, Kap95, Kap104, and Pse1 in presence of PR₅₀ or GA₅₀

Transport reporters	Wild type		PR ₅₀		GA ₅₀	
	N/C ^{*1} (no of cells)	N/C (no of cells)	Fold change to WT (log2) (p-value) ^{*2}	N/C (no of cells)	Fold change to WT (log2) (p-value) ^{*2}	
No NLS	1.24 \pm 0.14 (178)	1.24 \pm 0.15 (228)	0.01 (ns)	1.11 \pm 0.11 (115)	-0.16 (<0.0001)	
Ssb1 NES (Crm1)	0.53 \pm 0.15 (191)	0.47 \pm 0.16 (157)	-0.16 (0.0025)	0.62 \pm 0.22 (133)	0.22 (<0.0001)	
Sv40 NLS (Kap60/Kap95)	3.21 \pm 0.89 (156)	4.11 \pm 1.44 (207)	0.36 (<0.0001)	1.66 \pm 0.99 (108)	-0.96 (<0.0001)	
Npm1 NLS (Kap60/Kap95)	6.93 \pm 3.37 (146)	6.07 \pm 4.99 (130)	-0.19 (ns)	6.91 \pm 5.52 (142)	0.01 (ns)	
Nab2 NLS (Kap104)	7.59 \pm 2.82 (105)	6.37 \pm 2.42 (112)	-0.25 (<0.0001)	5.25 \pm 1.91 (105)	-0.51 (<0.0001)	
Pho4 NLS (Pse1)	5.37 \pm 2.71 (158)	2.82 \pm 1.10 (103)	-0.93 (<0.0001)	5.28 \pm 2.19 (151)	-0.01 (ns)	

*1 N/C: fluorescence in nucleus over fluorescence in cytosol; median \pm standard deviation

*2 ns= nonsignificant. Mann-Whitney test

1199

Table S3 Efflux rate constants of transport reporters in presence of PR₅₀ or GA₅₀

Transport reporters	Wild type		PR ₅₀		GA ₅₀	
	Efflux rate constant ^{*1} (no of cells)	Efflux rate constant ^{*1} (no of cells)	Fold change to WT (p-value) ^{*2}	Efflux rate constant ^{*1} (no of cells)	Fold change to WT (log2) (p-value) ^{*2}	

Sv40 NLS (Kap60/Kap95)	0.003 ± 0.001 (126)	0.002 ± 0.003 (125)	(<0.0001)	ND	ND
Nab2 NLS (Kap104)	0.001 ± 0.003 (254)	0.000 ± 0.001 (125)	(<0.0001)	0.004 ± 0.005 (139)	(<0.0001)
Pho4 NLS (Pse1)	0.003 ± 0.004 (188)	0.002 ± 0.003 (224)	(<0.0001)	0.005 ± 0.004 (124)	(0.0001)

*¹ Median ± standard deviation *² ns= nonsignificant, Mann-Whitney test *³ ND: not determined

1200

Table S4 Steady state localization of transport reporters for nuclear transport by Crm1, Kap95, Kap104, and Pse1 under stress conditions

Stress		Sv40 NLS (Kap60/Kap95)	Nab2 NLS (Kap104)	Pho4 NLS (Pse1)	Ssb1 NES (Crm1)
Wild type	N/C ^{*1} (no of cells)	5.32 ± 1.31 (97)	5.80 ± 2.25 (85)	5.39 ± 1.65 (95)	0.41 ± 0.12 (94)
5 minutes 37°C	N/C (no of cells)	4.92 ± 1.26 (97)	4.40 ± 1.37 (103)	4.51 ± 0.97 (95)	0.42 ± 0.12 (93)
	Fold change (p-value) ^{*2}	-0.11 (ns)	-0.40 (<0.0001)	-0.26 (<0.0001)	0.02 (ns)
1 hour 37°C	N/C (no of cells)	5.78 ± 2.60 (96)	6.20 ± 2.77 (101)	7.19 ± 2.43 (101)	0.45 ± 0.12 (103)
	Fold change (p-value)	0.12 (0.015)	0.10 (0.0062)	0.42 (<0.0001)	0.13 (ns)
5 minutes 42°C	N/C (no of cells)	4.81 ± 1.20 (91)	4.71 ± 1.71 (95)	5.24 ± 1.29 (93)	0.44 ± 0.12 (97)
	Fold change (p-value)	-0.15 (0.0026)	-0.30 (<0.0001)	-0.04 (ns)	0.10 (ns)
10 minutes 46°C	N/C (no of cells)	3.97 ± 1.41 (90)	9.77 ± 4.73 (88)	5.79 ± 1.94 (90)	0.54 ± 0.14 (98)
	Fold change (p-value)	-0.42 (<0.0001)	0.75 (<0.0001)	0.10 (ns)	0.39 (<0.0001)
Saturation	N/C (no of cells)	4.31 ± 1.31 (95)	4.98 ± 2.34 (98)	5.28 ± 1.43 (93)	0.65 ± 0.16 (101)
	Fold change (p-value)	-0.31 (<0.0001)	-0.22 (ns)	-0.03 (ns)	0.66 (<0.0001)
Water shift 24 hours	N/C (no of cells)	1.49 ± 0.41 (97)	2.02 ± 0.52 (85)	1.37 ± 0.39 (188)	0.45 ± 0.44 (97)
	Fold change (p-value)	-1.11 (<0.0001)	-1.91 (<0.0001)	-1.97 (<0.0001)	0.26 (<0.0001)
Osmotic shock control	N/C (no of cells)	5.09 ± 1.68 (91)	5.09 ± 2.07 (86)	5.84 ± 1.89 (92)	0.37 ± 0.10 (90)
	Fold change (p-value)	-0.06 (ns)	-0.19 (ns)	0.12 (0.0031)	-0.16 (0.0324)
NaPi shock	N/C (no of cells)	3.36 ± 1.27 (96)	3.12 ± 1.25 (95)	4.50 ± 1.58 (92)	0.41 ± 0.15 (86)
	Fold change (p-value)	-0.66 (<0.0001)	-0.90 (<0.0001)	-0.26 (0.0011)	0.00 (ns)
Osmotic shock	N/C (no of cells)	4.11 ± 2.04 (92)	4.80 ± 4.13 (90)	4.17 ± 2.09 (92)	0.77 ± 0.16 (94)
(Compared to osmotic shock control)	Fold change (p-value)	-0.31 (0.0022)	-0.08 (ns)	-0.49 (<0.0001)	1.06 (<0.0001)
5 minutes H ₂ O ₂	N/C (no of cells)	3.90 ± 1.52 (94)	3.23 ± 2.07 (85)	3.81 ± 1.15 (90)	0.43 ± 0.10 (88)
	Fold change (p-value)	-0.45 (<0.0001)	-0.85 (<0.0001)	-0.50 (<0.0001)	0.06 (ns)

30 minutes H ₂ O ₂	N/C (no of cells)	6.66 ± 2.45 (96)	6.24 ± 2.37 (92)	5.33 ± 1.80 (92)	0.44 ± 0.13 (92)
	Fold change (p-value)	0.32 (<0.0001)	0.11 (ns)	-0.02 (ns)	0.10 (ns)
Menadione	N/C (no of cells)	1.08 ± 0.27 (91)	1.00 ± 0.30 (78)	1.04 ± 0.34 (92)	0.86 ± 0.21 (78)
	Fold change (p-value)	-2.31 (<0.0001)	-2.53 (<0.0001)	-2.38 (<0.0001)	1.06 (<0.0001)
Ethanol	N/C (no of cells)	2.55 ± 0.99 (121)	2.72 ± 2.47 (122)	2.45 ± 0.90 (108)	1.06 ± 0.27 (101)
	Fold change (p-value)	-1.06 (<0.0001)	-1.09 (<0.0001)	-1.14 (<0.0001)	1.36 (<0.0001)

*¹ N/C: fluorescence in nucleus over fluorescence in cytosol; median ± standard deviation *² Fold change to wild type as Log2, ns= nonsignificant, Mann-Whitney test

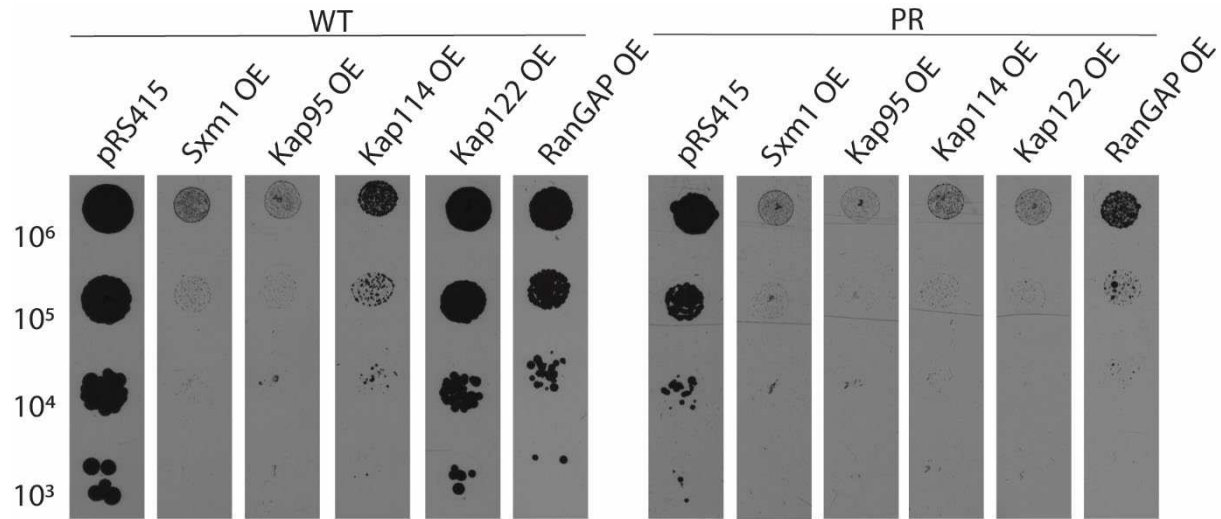
1201

Table S5 Steady state localization of transport reporters for nuclear transport by Crm1, Kap95, Kap104, and Pse1 cargos in mutants					
Stress		Sv40 NLS (Kap60/Kap95)	Nab2 NLS (Kap104)	Pho4 NLS (Pse1)	Ssb1 NES (Crm1)
Sxm1Δ	N/C (no of cells)	5.82 ± 2.21 (102)	6.56 ± 2.14 (100)	4.36 ± 1.20 (102)	0.40 ± 0.11 (94)
	Fold change (p-value) ^{*2}	0.39 (<0.0001)	-0.21 (0.0257)	-0.31 (<0.0001)	0.16 (0.0065)
Kap114Δ	N/C (no of cells)	5.01 ± 1.82 (98)	7.02 ± 4.44 (100)	4.71 ± 2.20 (102)	
	Fold change (p-value)	0.64 (<0.0001)	-0.11 (ns)	-0.19 (ns)	
Kap120Δ	N/C (no of cells)	5.39 ± 2.00 (78)	9.46 ± 3.98 (148)	7.30 ± 2.91 (153)	0.38 ± 0.12 (94)
	Fold change (p-value)	0.75 (<0.0001)	0.32 (<0.0001)	0.44 (<0.0001)	0.30 (<0.0001)
Kap122Δ	N/C (no of cells)	4.88 ± 2.00 (125)	4.21 ± 1.32 (209)	3.48 ± 0.98 (135)	0.39 ± 0.14 (96)
	Fold change (p-value)	0.61 (<0.0001)	-0.70 (0.0015)	-0.20 (0.0048)	0.30 (<0.0001)
Kap123Δ	N/C (no of cells)	4.04 ± 1.10 (73)	8.65 ± 2.26 (149)	3.29 ± 0.75 (110)	0.33 ± 0.07 (102)
	Fold change (p-value)	0.33 (<0.0001)	-0.65 (<0.0001)	-0.81 (<0.0001)	0.13 (0.0144)
RanGAP overexpression	N/C (no of cells)	4.35 ± 2.05 (100)	2.86 ± 1.59 (98)		0.46 ± 0.13 (91)
	Fold change (p-value)	-0.29 (0.0008)	-1.02 (<0.0001)		0.16 (ns)
RanGEF overexpression	N/C (no of cells)	4.00 ± 2.02 (97)	5.15 ± 1.67 (91)	4.35 ± 1.87 (95)	0.46 ± 0.15 (88)
	Fold change (p-value)	-0.41 (<0.0001)	-0.17 (0.0257)	-0.31 (<0.0001)	0.16 (0.0065)

*¹ N/C: fluorescence in nucleus over fluorescence in cytosol; median ± standard deviation *² Fold change to wild type as Log2, ns= nonsignificant, Mann-Whitney test

1202

1203



1204
1205 **Fig S2. Overexpression of NTRs is toxic to cells, additionally so with co-expression of PR₅₀. A)** Galactose induced
1206 overexpression of NTRs Sxm1, Kap95, Kap114 is toxic to cells; overexpression of Kap122, and RanGAP, is less toxic (left panel).
1207 Simultaneous galactose induced co-expression of PR₅₀, is lethal for all NTRs and RanGAP OE.